Sol-gel synthesis of nanocrystalline MgO and its application as support in Ni/MgO catalysts for ethanol steam reforming

Luiz G Possato, Rosembergue G L Gonçalves, Rodrigo M M Santos, Thiago F Chaves, Valérie Briois, Sandra H Pulcinelli, Leandro Martins, Celso V Santilli

Sol-gel synthesis of nanocrystalline MgO and its application as support in Ni/MgO catalysts for ethanol steam reforming

Luiz G. Possato[a,b]*, Rosembergue G. L. Gonçalves[a], Rodrigo M. M. Santos[a], Thiago F. Chaves[a], Valérie Briois[b], Sandra H. Pulcinelli[a], Leandro Martins[a] and Celso V. Santilli[a]

[a] *Universidade Estadual Paulista (Unesp), Instituto de Química, Campus de Araraquara, Rua Prof. Francisco Degni 55, 14800-060 Araraquara, SP, Brazil*

[b] *Synchrotron SOLEIL, L'Orme des Merisiers, BP48, Saint Aubin, 91192 Gif-sur Yvette, France*

Abstract

This work reports the improved catalytic activity of nickel catalysts supported on nanocrystalline magnesium oxide prepared by a sol-gel method, with Pluronic P123 used as a structure-directing agent for pore formation. The presence of Pluronic also provided a reduction of the magnesium oxide crystallite size from 54 to 18 nm, as well as the attainment of small supported metallic nickel particles. *In situ* X-ray diffraction was used to assess the structural evolution of the materials during activation, followed by analyses using X-ray absorption spectroscopy, N_2 physisorption isotherms, transmission electron microscopy, and temperature-programmed CO_2 desorption. The materials synthesized with the surfactant presented heightened activity in the ethanol steam reforming reaction. The long-term stability of the catalysts was improved, due to suppression of the total quantity of coke, with the catalyst prepared using surfactant developing less deactivating coke.

Keywords: MgO, sol-gel, nickel catalysts, ethanol steam reforming, coke formation.

*Corresponding author: gustavo.possato@unesp.br

1. Introduction

The production and storage of energy are indispensable for the maintenance of modern society [1], while the use of renewable sources is crucial for decreasing the environmental impacts caused by fossil fuels. Consequently, a focus of research attention is the development of suitable catalytic materials for the conversion of renewable substrates into fuels and energy [2–4]. In several countries, sugarcane stands out as a source of fuel ethanol, while also often providing a surplus of electricity. Furthermore, biomass-derived ethanol is important in the production of hydrogen for use in high efficiency electricity fuel cells, which is a clean process with water as the only byproduct [5–7].

Currently, hydrocarbon steam reforming reactions are the most common and economically competitive way of obtaining hydrogen [8], so the development of suitable supports and catalysts for the abstraction of hydrogen from ethanol is environmentally appealing. Ethanol steam reforming is an endothermic reaction (ΔH of 347.4 kJ/mol) that produces 6 moles of hydrogen per mole of ethanol (Eq. 1) [9].

$$CH_3CH_2OH + 3H_2O \rightleftharpoons 6H_2 + 4CO_2 \qquad \text{(Eq. 1)}$$

In general, the reforming of organic compounds such as ethanol into hydrogen and carbon dioxide is performed using catalysts based on noble metals such as rhodium, or non-noble metals such as nickel and cobalt [10–14]. MgO, Al_2O_3, ZnO, CeO_2, and La_2O_3 are common supports [4,8], but depending on the overall preparation procedures, they may present textural or physicochemical properties that lead to low performance [15]. For instance, Al_2O_3 is a suitable support for several catalytic reactions, because its high surface area promotes the dispersion of metallic particles. However, its acidity allows the occurrence of undesirable parallel reactions, such as ethanol dehydration to produce ethane, with subsequent oligomerization resulting in the formation of coke, which is one

of the factors causing catalyst deactivation [8]. In the case of nickel supported on Al_2O_3, coking is likely to initiate on larger nickel particles, with faster aggregation, compared to smaller metallic particles [9].

There is a need to develop catalyst supports with high surface area and porosity, in order to allow the creation of small particles and the provision of satisfactory acid/base properties. We previously studied the synthesis of porous MgO by combining sol-gel transition with use of the Pluronic P123 surfactant as a structure-directing agent [16]. MgO presents appropriate basicity for improving catalyst performance and avoiding undesirable parallel reactions during ethanol steam reforming [8]. The activity of metallic sites in the conversion of ethanol to acetaldehyde, the first step of the ethanol steam reforming reaction, is enhanced because of the interactions with basic sites [17]. MgO is also less prone to the formation of oligomeric carbon species on the surface, due to the competing adsorption of water. Carbonaceous compounds decompose before polymerization on the catalyst surface [18]. Synthesis using the Pluronic P123 surfactant allows control of the MgO crystallite size and surface area, together with improvements in the quantity and strength of basic sites [19–23].

In the present work, we show that the use of Pluronic P123 as a structure-directing agent in the synthesis of MgO affects its porous structure. The modified textural properties of the support lead to the dispersion of nanocrystallites of nickel species, consequently affecting the production of hydrogen by ethanol steam reforming. During the nickel reduction, time-resolved synchrotron radiation measurements (X-ray diffraction and X-ray absorption) and temperature-programmed reduction (TPR) were used to assist in elucidation of the structures and the active species formed using the modified supports. The effect of nickel loading on activity and product distribution was investigated, together with the deactivation behavior. Investigation of the spent catalysts

using N_2 physisorption, transmission electron microscopy (TEM), thermogravimetry (TG), and differential thermal analysis (DTA) provided further understanding of the properties of the catalysts.

2. Experimental

2.1. Synthesis of catalyst supports

The MgO was prepared using a sol-gel procedure, in the presence of Pluronic P123 surfactant, as described previously [16], adapted from Rezaei *et al.* [21]. Firstly, 0.47 g of the surfactant was solubilized in 3 mL of water, at 60 ºC, under mechanical stirring at 500 rpm. To this solution, 2.56 g of $Mg(NO_3)_2.2H_2O$ was added and completely solubilized. Next, the addition of 5 drops of NH_4OH (28%) increased the pH to 10, resulting in sol-gel transition. The gel was dried at 60 ºC for 24 h. The dried powder was calcined in a muffle oven, under an air atmosphere, using a heating rate of 1 ºC/min up to 190 ºC, maintaining this temperature for 2 h, followed by a second heating step at 1 ºC/min up to 600 ºC, maintaining the final temperature for 2 h. Use of Pluronic P123/MgO molar ratios of 0.008 and 0.032 resulted in the samples denoted P1 and P2, respectively. A reference sample synthesized without Pluronic was denoted P0.

2.2. Impregnation of the supports

The impregnated samples containing 1 and 10 wt.% of nickel were prepared by wet impregnation using $Ni(NO_3)_2.6H_2O$ (Sigma-Aldrich) as a nickel source. 1 g of the support and 50 mL of water were mixed with the $Ni(NO_3)_2.6H_2O$, under stirring for 1 h at room temperature, followed by removal of the water in a rotary evaporator. After calcination, the samples containing 1 and 10 wt.% of nickel were denoted $Ni_{01}P0$ and $Ni_{10}P0$, respectively. For the P1 and P2 supports, addition of 10 wt.% of nickel resulted

in the samples $Ni_{10}P1$ and $Ni_{10}P2$. Subsequent calcination of the samples was performed by heating in a muffle oven at 600 ºC for 2 h (ramp rate of 10 ºC/min), under an air atmosphere.

2.3. Characterization of the catalysts

The crystalline phases of the samples were identified by powder X-ray diffraction (XRD), using a Siemens D5000 diffractometer, with Cu Kα radiation selected by a curved graphite monochromator. Data were collected in the 2θ range from 5 to 100º, with a scan step of 0.01º and counting time of 4 s.

Thermal activation was monitored by *in situ* XRD and XAS (X-ray absorption spectroscopy) analyses. For both experiments, the calcined samples were heated from room temperature (25 °C) up to 600 ºC, at a rate of 10 ºC/min, maintaining the final temperature for 1 h, under a constant gas flow of 5% H_2 in He, at 60 mL/h. *In situ* XRD analysis was performed at the XPD beamline of the Brazilian Synchrotron Light Laboratory (LNLS). The XPD beamline had a Huber 4+2 circle diffractometer equipped with an Eulerian cradle (model 513), positioned 13 m from a double-bounce Si(111) monochromator (10 keV) [24,25]. This energy region was selected to improve the number of reflections up to 100 2θ (°) and to provide greater accuracy in the refinement analysis. An Arara furnace (developed in-house at LNLS) was used to heat the samples. Quantitative phase analysis was performed by the Rietveld profile method, using MAUD software [26,27]. The scale factors, zero shifts, backgrounds of the peak profiles, and the lattice parameters were refined using a sixth-degree Chebyshev polynomial. Pseudo-Voigt functions were employed for the peak profile refinements. Other parameters were not refined.

In situ time-resolved X-ray absorption spectroscopy (XAS) analyses were performed at the ROCK beamline of the SOLEIL synchrotron, in transmission mode, at the nickel K-edge (8333 eV), using the Quick-EXAFS capability [3,28]. An Si(111) channel-cut crystal was tuned to a Bragg angle of 2.4°, near to the Ni K-edge energy. A frequency of 2 Hz was selected for the crystal oscillation, allowing the acquisition of 4 spectra per second, each of 0.25°s. Consecutive spectra saved during 10 s were merged in order to improve the signal/noise ratio. Normalization of the data was performed using the Python normal_gui graphical interface, developed at SOLEIL for huge amounts of Quick-EXAFS data [29]. The sample (20 mg) was prepared with 20 mg of boron nitride (BN) and the mixture was placed in a 2 mm-thick stainless steel cavity, with a dedicated catalytic reactor connected to the gas feeding system of the beamline [30]. The outflowing gases were monitored using a coupled mass spectrometer (Cirrus, MKS).

Analysis of the XANES data was performed with Athena graphical interface software [31]. The spectra were normalized using the flattening algorithm in the default energy range used by Athena. Speciation of the nickel during the *in situ* treatments was achieved by linear combination (LC) of the XANES spectra (from -20 to 120 eV around the edge). All the references used for LC were heated using the same heating rate as the samples, in order to provide linear combinations with the same temperature (reference/sample) and overcome resonance damping from thermal vibrations. Commercial NiO, metallic nickel foil, and NiMgO solid solution were used as references. The NiMgO solid solution reference was obtained by heating a sample containing 1% nickel to 600 °C, maintaining isothermal treatment at this temperature for 2 h.

The EXAFS oscillations were extracted from the normalized Ni K-edge Quick-XAS data using the Athena graphical interface software [31]. The EXAFS data were Fourier transformed using a k^3-weighting Kaiser-Bessel window (dk = 1) over the 4.2-10.3 $Å^{-1}$ k-range. EXAFS fitting of distances, coordination numbers, and Debye-Waller factors was performed with the Artemis interface to IFeFFIT, using least-squares refinements that were firstly checked using a metallic nickel foil reference.

Considering the metallic nickel as an icosahedral model [32] and using the EXAFS results, it was possible to extract the dispersion (Disp.) particle size employing the EXAFS signal ($D_{Ni\ EXAFS}$) and metallic surface area (S_{met}) determinations, as follows:

$$N_{Ni-Ni} = \frac{6L(20L^2+15L+7)}{10L^3+15L^2+11L+3} \qquad \text{(Eq. 2) [33,34]}$$

$$Disp. = \frac{30L^2+6}{10L^3+15L^2+11L+3} \qquad \text{(Eq. 3) [33,34]}$$

$$D_{Ni\ EXAFS} = \frac{600W_{Ni}}{Disp.N_a\rho\sigma} \qquad \text{(Eq. 4) [35,36]}$$

$$S_{met} = 0.065xCxDisp. \qquad \text{(Eq. 5) [37]}$$

where, N_{Ni-Ni} is the coordination number obtained from EXAFS, L is the nickel cluster order, N_a is the Avogadro number ($6.02x10^{23}$), ρ and W_{Ni} are the metal density (8.91 g/cm^3) and the molecular weight of the metal (58.69 g/mol), respectively, and σ is the surface area per nickel atom ($6.52x10^{-16}$ cm^2/atom) [36]. C is the metallic concentration, considering only the reduced quantity.

Temperature-programmed reduction (TPR) was performed using an Autochem 2910 instrument (Micromeritics) equipped with a TCD detector. A mass of 100 mg of the sample was placed in a quartz sample holder and pretreated under a 30 mL/min flow of 5% O_2 in He, to eliminate impurities, with heating (at 10 °C/min) from room temperature (25 °C) to 400 °C, maintaining the final temperature for 30 min. After

cooling to room temperature, the sample was purged during 5 min with a 30 mL/min flow of He and the TPR analysis was performed up to 1000 °C, with heating at 10 °C/min, under a 30 mL/min flow of 10% H_2 in Ar. The TPR quantification was obtained by integration of the peaks and comparison to an analytical curve.

Nitrogen adsorption-desorption isotherms were recorded at liquid nitrogen temperature (~77 K), in the relative pressure interval between 0.002 and 0.998, using a Micromeritics ASAP 2010 physisorption system. Before the measurements, the samples were degassed at 200 ºC for 12 h, under a vacuum of 10 μPa. The Brunauer-Emmett-Teller (BET) equation was used to calculate the specific surface area [38]. The BJH method was used for determination of the pore distribution [39].

The basicity of the samples was evaluated by temperature-programmed desorption of CO_2 (TPD-CO_2). A mass of 100 mg of the sample was heated to 600 ºC, at 20 ºC/min, under a 50 mL/min flow of He. The final temperature was maintained for 1 h, to eliminate adsorbed impurities. The furnace was then cooled to 100 ºC and CO_2 was fed at 60 mL/min for 1 h. The purge step was performed with He (30 mL/min) for 1 h, followed by heating to 600 ºC, at 10 ºC/min, for desorption. The CO_2 desorption event was monitored at m/z = 44, using a Pfeiffer PrismaPlus QMG 220 mass spectrometer.

Transmission electron microscopy (TEM), employing an FEI-TECNAI LaB6 instrument operating at 200 kV, was used to analyze the nanostructure and the dispersion of the nickel species. The samples were prepared for TEM by wetting formvar/carbon film-coated copper TEM grids with a drop of the colloidal alcoholic suspensions, followed by drying in air. The distribution of the crystalline phases was determined using CIF files and an ASTAR NanoMegas system. After acquisition of the TEM images, the same grids with the samples were submitted to mapping of the nickel

species by electron diffraction, and CIF file standards (MgO, NiMgO, NiO, and Ni) were used for comparison with the results obtained. Operation of the ASTAR NanoMegas system was performed by scanning the electron beam (in nanoprobe mode) on the sample area and using a charge-coupled device (CCD) camera to obtain a high number of electron diffraction spot patterns (on the order of thousands of patterns) to be subsequently indexed automatically by template matching (using the CIFs) [40].

The formation of coke on the spent catalysts was observed by scanning electron microscopy (SEM), using a JSM7500F microscope (JEOL). The samples were previously suspended in isopropanol, deposited on a silicon sample holder, dried, and sputter-coated with gold.

2.4. Catalytic tests

For the ethanol steam reforming reaction, masses of 100 mg of catalyst were activated and the reaction was performed at different temperatures between 400 and 600 °C. The feed composition was a mixture of ethanol/water in He (5% ethanol, 10% water, and 85% He), at a flow rate of 60 mL/min. For the isothermal tests, the temperature was fixed at 500 ºC and the reaction was monitored during 6 h. The outflow compounds were evaluated using a Pfeiffer PrismaPlus QMG 220 mass spectrometer, with monitoring of m/z 44, 43, 31, 28, 26, 15, 2, and 4, for CO_2, CH_3CHO, CH_3CH_2OH, CO, C_2H_4, CH_4, H_2, and He, respectively. The signals were compared to those for standard gases. The fragments of other chemical species were subtracted, as well as the background [41].

The ethanol conversion and the distribution of the products were calculated according to Eqs. 6 and 7, respectively:

$$X_{ethanol}\ (\%) = \frac{n_{et}^{input} - n_{et}^{output}}{n_{et}^{input}}\ x\ 100 \qquad \text{(Eq. 6)}$$

$$P_{Di}\ (\%) = \frac{n_i}{\sum n_{All}}\ x\ 100 \qquad \text{(Eq. 7)}$$

where, n_{et}^{input} and n_{et}^{output} are the molar flows of ethanol in the input and output, n_i is the molar flow of product i, and n_{All} is the sum of the molar flows of all the products.

Thermogravimetric analysis (TGA) and differential thermal analysis (DTA) were carried out under nitrogen or oxygen flows (100 mL/min), using an SDT Q600 TGA/DSC thermobalance (TA Instruments), in order to evaluate the coke deposits on the spent catalysts. The sample was heated from 30 to 600 ºC, at a rate of 10 ºC/min, under a flow of air (100 mL/min).

3. Results

3.1. Structural features

The X-ray diffractograms of the calcined samples (Fig. 1a) revealed the greatest intensities for the (200), (220), and (222) peaks related to the MgO periclase structure (ICSD - *Inorganic Crystal Structure Database* 9863) [42]. The assessment of nickel-based phases was not possible, because the diffraction patterns of NiO (ICSD 9866) and NiMgO (ICSD 290603) were very similar to that for the MgO periclase structure. For fine-tuned analysis, quantitative phase analysis was performed by the Rietveld method (the refined diffractograms are shown in Fig. S1), which resulted in only the $Ni_{10}P0$ sample presenting 10% of crystalline NiMgO. NiO was also searched in the refinement analysis, but was not observed for any sample. Since the XRD patterns of MgO and NiMgO were similar (Fig. S2a), *in situ* XRD measurements were performed at 10 keV, rather than at the more conventional 8 keV energy (approximately Cu Kα; Fig. 1a), in order to increase the number of diffraction peaks in the diffractogram and improve the quality/reliability of the refinement analysis. Fig. S2b illustrates the theoretical difference in the peak positions for the (200) plane 4.22 Å cell parameter of MgO and the 4.18 Å cell parameter of NiMgO. The intensity maximum of the $Ni_{10}P0$ peak was shifted to a larger angle than the position calculated for MgO, indicating the presence of a quantity of NiMgO (10%, as revealed by the Rietveld refinement). A similar difficulty was reported by Wurzler *et al.* [43].

The diffractograms for the samples prepared with Pluronic presented reduced intensity and broadening of the peaks, caused either by decrease of the crystallite size or by increase of the lattice microstrains. The full width at half maximum (FWHM) of the (002) peak was used to calculate the average crystallite size, employing the Scherrer equation [44]. The results (Table 1) indicated that the addition of Pluronic limited MgO crystallite growth, allowing a progressive decrease of the average crystallite size from 54 nm ($Ni_{10}P0$) to 18 nm ($Ni_{10}P2$), with suppression of some diffraction peaks. Due to the strong decrease of crystallinity for the samples prepared with Pluronic, the presence of the NiO and NiMgO phases could not be assessed from the Rietveld refinements.

Although the samples showed no detectable nickel oxide crystalline phases, the change of the MgO cell parameters for all the catalysts suggested dissolution of the nickel atoms on the periclase lattice and the formation of a solid solution (Table 1). The X-ray absorption spectroscopy (XAS) technique, with atomic selectivity, was used to study the local order structure of the nickel atoms and to confirm their dissolution in the periclase structure. The concentrations of the different nickel species were determined using the linear combination of spectra corresponding to standard compounds (Ni, NiO, and NiMgO) (Fig. 1b). This quantitative procedure indicated that the nickel atoms were only in solid solution for the $Ni_{01}P0$ sample, while for the $Ni_{10}P0$ sample, NiMgO and NiO coexisted in equivalent amounts (Table 1). This was consistent with the systematic study of the Ni/MgO system reported by Wang *et al.* [45], which showed increasing formation of NiO with increase of the nickel loading from 3.4 to 45 wt.%, where the sample containing 3.4 wt.% Ni and calcined at 600 °C presented only the NiMgO solid solution. In the process of catalyst activation with hydrogen, reduction of the nickel atom often occurs at lower temperatures for NiO, compared to NiMgO [45]. Section 3.2

provides details of the speciation of nickel and the evolution of the species during activation of the catalysts.

Table 2 presents the textural properties of the samples, determined from the N_2 adsorption/desorption isotherms (Fig. S3). The curves for all of samples were characteristic of type II isotherms, according to the IUPAC classification, displaying a continuous increase of N_2 adsorption at a high relative pressure ($P/P_0 \approx 1$), typical of macroporous materials [46,47]. However, the near-vertical hysteresis loop (type H1), observed for all the samples, indicated the coexistence of mesopores. The type H1 hysteresis is often associated with porous materials consisting of cylindrical-like pore channels between approximately uniform particles [46]. For the $Ni_{01}P0$ sample, the hysteresis also displayed a nearly horizontal component, evidencing the additive contributions of H1 and H4 loops. The H4 hysteresis is often associated with narrow slit pores formed by plate-like particles [46]. The addition of an increasing amount of surfactant resulted in progressive increases of the adsorbed N_2 volume and the H1 hysteresis loop, indicative of increased mesoporosity. In agreement with the hysteresis loop features, the pore size distributions obtained by the BJH method [39] showed bimodal mesopore size distributions for the $Ni_{01}P0$ and $Ni_{10}P2$ samples, while the distributions were monomodal for the $Ni_{10}P0$ and $Ni_{10}P1$ samples (Fig. 2). The absence of the smaller pore size family for the samples prepared with a higher amount of nickel and a lower amount of surfactant (samples $Ni_{10}P0$ and $Ni_{10}P1$) suggested that the nickel species acted to block the narrow slit-like pores [48]. Furthermore, the increasing addition of surfactant led to continuous growth of the size of the H1 pores family. As a consequence of the concurrent effects of the additions of surfactant (pores directing) and nickel (pores blocking), the $Ni_{10}P1$ sample displayed the highest specific area and pore volume, with values of 57 m^2/g and 0.50 cm^3/g, respectively (Table 2).

The Pluronic P123 surfactant is often used as an amphiphilic template agent because of its high molecular weight (5800 g/mol), which generates materials with relatively large mesopores and thick inorganic walls, conferring greater stability to the material, compared to the use of low molecular weight surfactants [49]. Furthermore, the addition of macromolecules such as polymers in the sol-gel synthesis is also reflected in the aggregation of particles. The polymers adsorbed on the inorganic surface act as a protective layer, with the accumulation of surfactant between two particles, for example, favoring interpenetration of the solvent (by osmosis), facilitating the separation of the particles. The particle morphology is dependent on the surfactant concentration and the synthesis condition. Therefore, the Pluronic P123 acts as both a dispersant and a structure-directing agent.

As discussed above, the use of Pluronic in the sol-gel synthesis led to the smallest MgO crystallites. The $Ni_{01}P0$ and $Ni_{10}P2$ samples presented bimodal pore size distributions, while monomodal distributions were observed for $Ni_{10}P0$ and $Ni_{10}P1$. In general, the use of a surfactant in sol-gel synthesis leads to the formation of cylindrical, vermicular, and lamellar organized pores [50–52]. In synthesis with Pluronic P123 and magnesium salts, the creation of slit pores is favored, as observed by Rezaei *et al.* [21,49] and Zanganeh *et al.* [53], in agreement with the results obtained in this study.

3.2. Activation of the samples

The activation of the calcined samples, monitored using *in situ* XRD, was achieved by heating the samples to 600 ºC under a flow of 5% H_2 in 95% He (Figs. 3 and S4). In the case of the $Ni_{10}P0$ sample, the diffraction peak related to metallic nickel appeared after heating above 500 °C (Fig. 3a). However, the diffractograms for $Ni_{10}P2$, $Ni_{01}P0$, and $Ni_{10}P1$ (Figs. 3b, S4a, and S4b, respectively) did not display the metallic

nickel diffraction peak, which could be explained by a negligible amount of metallic crystalline phase or a tiny crystallite size. However, the normalized full width at half maximum (β/β_{max}) of the (002) reflection of periclase revealed an attenuation between 300 and 350 °C, for all the samples, which was more pronounced for $N_{10}P1$ and $Ni_{10}P2$ (Fig. 3c). This evidenced a release of lattice microstrains, probably related to mixing-demixing of nickel atoms in NiMgO solid solution. The NiO reference sample (Fig. S3c) also showed initiation of the reduction of NiO at 300 °C. These results indicated that the non-homogeneous distribution of nickel atoms, dissolved in higher concentrations at the boundaries of the NiMgO crystallites, was the driving force for microstrain relaxation induced by localized stress. The XRD results were corroborated by the nickel speciation, as monitored by *in situ* XANES during the activation.

Fig. S5 shows the time-resolved XANES spectra at the Ni K-edge during the activation under heating to 600 ^{o}C. In the case of the $Ni_{01}P0$ calcined sample (Fig. 4a), which contained only the nickel atoms in the form of NiMgO, a minor quantity of metallic nickel started to appear at ~400 °C, leading to 10% of Ni^0 after 1 h at 600 ºC. For the $Ni_{10}P0$ sample obtained after calcination of 30% of NiO and 70% of NiMgO (Fig. 4b), the demixing process started at 320 °C, as shown by the XRD analysis, while the onset of reduction occurred above 570 °C, leading to ~10% of the metallic nickel species. The formation of NiO and the higher reduction temperature, compared to the $Ni_{01}P0$ sample, were due to the higher nickel loading and consequently decreased dispersion of the nickel atoms. The increase of the EXAFS coordination number for the Ni contribution at 2.48 Å, characteristic of the Ni^0 species, was indicative of the sintering of metallic nickel domains (Table S1). For the $Ni_{10}P1$ and $Ni_{10}P2$ samples prepared with Pluronic (Figs. 4c and 4d), the stepped formation of metallic nickel started at lower temperatures of 480 and 440 °C, with the demixing processes occurring

at 300 and 220 °C, respectively. The textural properties conferred by the sol-gel synthesis with Pluronic assisted the lability of nickel atoms from the mixed oxide, contributing to greater nickel reduction. The two samples prepared with Pluronic reached similar amounts (~20%) of reduced nickel atoms.

Separate TPR measurements (Fig. S6) also indicated the reduction events observed by XAS. The $Ni_{01}P0$ sample showed no reduction below 400 °C (Region 1, Fig. S6), confirming the lack of NiO [45,54], in agreement with the XAS results. The main reduction peak centered at 670 °C (Region 2) suggested that the nickel atoms were located on the surface or in subsurface layers associated with MgO in a non-homogeneous solid solution [45,54]. In Region 3, after 900 °C, a small H_2 consumption signal indicated the presence of some nickel atoms in the bulk material, associated with MgO in a solid solution. For $Ni_{10}P0$, the H_2 consumption evidenced above 200 °C suggested the presence of NiO, with the highest peak in Region 1 being associated with nickel on the surface or in subsurface layers [45,54]. For the samples prepared with the surfactant, NiO reduction was also observed at 450 and 430 °C for $Ni_{10}P1$ and $Ni_{10}P2$, respectively. However, most of the nickel atoms were in the form of Ni-MgO solid solution, being reduced above 700 °C for both samples [45,54]. The reducibility of the samples also revealed the effects related to dispersion of nickel in the support (Table 3). For $Ni_{01}P0$ and $Ni_{10}P0$, the nickel was completely reduced, while for the samples prepared with the supports (P1 and P2), the nickel atoms were partially reduced. The constant consumption of H_2 in Region 3, with peaks at different temperatures, indicated that various Ni species were formed as a consequence of the diffusion of nickel into the support, from the outermost layer to the subsurface layer, and then to the inner lattice [55].

The TEM images revealed nickel atoms (dark particles) on a 400 nm block crystal of MgO, for the $Ni_{10}P0$ sample (Fig. S7a). For the $Ni_{10}P2$ sample (Fig. S7b), small particles of nickel species could be seen, together with small crystallites of the support, in agreement with the XRD results. As observed by XANES, the nickel species appeared as metallic nickel, nickel magnesium oxide, and nickel oxide. Hence, it was difficult to attribute the particles in the dark region of the TEM images exclusively to metallic nickel species. Therefore, a mapping of these nickel compounds was performed (Fig. 5a). The nickel species were less homogeneously distributed in $Ni_{10}P0$, compared to $Ni_{10}P2$. The metallic nickel particle size was smaller for $Ni_{10}P2$, in agreement with the *in situ* XRD results. However, the size distributions were entirely different for the samples prepared with and without Pluronic. The average sizes of the metallic particles in the $Ni_{10}P0$ and $Ni_{10}P2$ catalysts were 20 and 6 nm, respectively (Fig. 5b). Hence, despite significant solid solution formation in the $Ni_{10}P2$ sample, as shown by XAS, a higher number of smaller metallic particles were obtained, compared to the $Ni_{10}P0$ catalyst. Similar behavior was reported by Asencios *et al.* [56], who found that the solid solution promoted fine dispersion of nickel metal and inhibited the formation of large clusters of Ni^0.

In summary, these sets of results indicated the crucial roles of the nickel loadings and the porous texture on the distribution of nickel atoms in the support, bulk and superficial nickel oxide, and NiMgO solid solution. Low nickel concentration and small MgO crystallite size favored NiMgO formation, according to the *in situ* XRD and XAS analyses. Smaller crystallite size, together with the high specific surface area and mesoporosity induced by the addition of Pluronic, favored the formation of a greater number of small metallic particles, due to the facilitated interaction of nickel species with the MgO support.

3.3. Catalytic activity

The activities of the catalysts in the steam reforming of ethanol (Fig. 6a) were evaluated during 1 h, using temperatures from 400 to 600 °C. The activities differed, especially at the lowest reaction temperature. The $Ni_{01}P0$ catalyst, despite having the lowest nickel loading, promoted higher conversion of ethanol of approximately 60%, compared to the 20% conversion achieved with $Ni_{10}P0$. This behavior was related to both the dispersion and the particle size of the active phase. A feature common to $Ni_{01}P0$ and $Ni_{10}P0$ was the reduced conversion in the first hour of reaction.

At 450 °C, the conversion increased for both catalysts, more markedly for $Ni_{10}P0$, which also showed greater deactivation. Despite the higher quantity of metallic species for $Ni_{10}P0$, as determined by XAS, the size of the particles hampered high catalyst stability. Similar behavior persisted for other temperatures. For instance, from 450 to 500 ºC, the conversion increased for both catalysts, but the activity decreased more significantly for $Ni_{10}P0$. At 550 °C, $Ni_{01}P0$ showed higher conversion (above 80%), while $Ni_{10}P0$ provided ethanol conversion of around 70%. At 600 °C, the conversions were similar, at approximately 90%. As expected, the results highlighted the critical role of the dispersion of metallic species in influencing stability and catalytic conversion.

The $Ni_{10}P1$ and $Ni_{10}P2$ catalysts were much more active than $Ni_{01}P0$ and $Ni_{10}P0$ (Fig. 6a). The catalysts prepared with surfactant showed conversions near 90%, even at the lowest temperature, highlighting the effectiveness of Pluronic P123 in the synthesis of the support. The conversion of ethanol also increased when the temperature was raised, reaching 100% at 600 °C.

The product distributions were similar for all the catalysts (Figs. 6b, 6c, and S8), with the reaction temperature being the most determinant parameter. For $Ni_{01}P0$ (Fig. 6b), hydrogen accounted for 70% of the products at 400 °C. The selectivity to hydrogen improved when the temperature was increased, reaching 90% at 600 °C. However, above 500 °C, the selectivity to CO started to grow proportionally with temperature. It is known that CO can participate in reactions responsible for deactivation of catalysts [57]. For this reason, the stability tests (discussed in the next section) were performed at 500 °C. The importance of using catalysts with alkaline properties is also related to the avoidance of parallel reactions, such as the ethanol dehydration that produces ethene, which is responsible for coke formation [18]. The formation of ethene was suppressed for all the catalysts, with around 0% at 500 °C. The product distributions for the $Ni_{10}P0$, $Ni_{10}P1$, and $Ni_{10}P2$ catalysts were similar to that for the $Ni_{01}P0$ catalyst. For one of the most active catalysts, $Ni_{10}P2$ (Fig. 6c), the CO_2 content was very low at 400 °C, due to the production of CO, CH_4, and ethylene, whose signals were more intense, for example compared to the $Ni_{10}P0$ catalyst (Fig. 6b).

The ethanol steam reforming reaction is known to present several parallel reactions that depend on the flow conditions, the composition of reagents, and the type of catalyst used. The reaction temperature is also a determining factor, since it affects the equilibrium constants of the primary and parallel reactions. Hence, many products may not come directly from the steam reforming reaction, but from the parallel reactions, each with its own stoichiometry. For this reason, calculations were made of the product distribution, rather than the selectivity to products.

Several studies [8,58–60] have evaluated the thermodynamic aspects of the reactions related to ethanol steam reforming. For example, the water-gas shift reaction, with the conversion of carbon monoxide and water into carbon dioxide and molecular

hydrogen, is an exothermic reaction that is favored at low temperatures. This explains why the carbon monoxide component increased from 500 °C up to 600 °C. Table S2 shows a set of reactions that can occur during ethanol steam reforming.

The structural parameters obtained from fitting of the EXAFS spectra recorded during the catalytic reactions were useful for explaining the different efficiencies of the catalysts (Table S1, Fig. 7). For the $Ni_{10}P0$ catalyst, the coordination number (N) of 9.4 for the Ni-Ni bond, related to the short metal distance (~2.5 Å), was much higher than for the samples prepared with Pluronic and for the $Ni_{01}P0$ catalyst (average N = 6), suggesting that the metallic particles found in these catalysts were also smaller. Another notable feature of these results was the high Ni-Ni coordination number (4.7) for the distance in the oxide (~2.9 Å) for $Ni_{10}P0$, with values below 1 for the other samples. This higher value encompassed the NiO contribution, as observed in Fig. 4, and was related to the lower Ni dispersion. The EXAFS results also enabled estimation of the dispersion (Table S3), evidencing the remarkable increase from 55% ($Ni_{10}P0$) to 89 and 87% for the samples prepared with Pluronic ($Ni_{10}P1$ and $Ni_{10}P2$, respectively). Accordingly, the metallic surface area (S_{met}) for the samples prepared with Pluronic increased 3-fold, compared to $Ni_{10}P0$, while the turnover frequency (TOF) calculated at 500 °C was enhanced 5-fold.

Another interesting observation was the effect of nickel loading and the dispersion of active sites. Although the $Ni_{01}P0$ catalyst contained only 10% of metallic nickel atoms, the ethanol conversion was higher than obtained with the $Ni_{10}P0$ catalyst. This finding evidenced the dominant role of the size of the metallic particles, which were formed by only 13 Ni atoms in $Ni_{01}P0$ and by 252 atoms in $Ni_{10}P0$. Furthermore, although the metallic area was increased in the samples prepared with Pluronic, TOF was increased even more, showing a beneficial relationship with the structure of the

support. In accordance with the best dispersion revealed from the TEM (Fig. 6) and EXAFS results, the nickel particles present in $Ni_{10}P2$ provided higher catalytic conversion, even at 400 °C.

3.4. Stability and analysis of the spent catalysts

The $Ni_{10}P0$ and $Ni_{10}P2$ catalysts were submitted to isothermal testing at 500 °C (Fig. 8a), in order to show the effects for conversion with the same nickel loading during 6 h of reaction. The $Ni_{10}P0$ catalyst showed a decrease of catalytic conversion, mainly during the first two hours on stream, with 47% deactivation after 6 h of reaction (Table 4). The $Ni_{10}P2$ catalyst converted more ethanol over the whole period, with lower deactivation (7%). Irrespective of the catalyst, the metallic nickel remained constant during the first three hours of the reaction (Fig. 4), demonstrating that the deactivation was not related to re-oxidation of the metal.

Thermogravimetric analyses of the spent catalysts enabled understanding of the benefit of incorporation of the nickel species on the supports prepared with surfactant (Fig. 8b). The mass losses for the $Ni_{10}P0$ and $Ni_{10}P2$ catalysts were 16 and 9%, respectively (Table 4). For $Ni_{10}P2$, the decomposition of the coke species started at a lower temperature, compared to $Ni_{10}P0$, as evidenced in the dTG curve (Fig. 8b). For $Ni_{10}P0$, The maximum rate of the main event was located at 515 °C while for $Ni_{10}P2$, two different events were located at 340 and 430 °C. The coke formed from reforming reactions can present four species: (1) monoatomic adsorbed carbon (C_α), which has no influence on catalyst deactivation and decomposes at ~340 °C; (2) amorphous polymeric films (C_β), which decompose at ~450 °C; (3) vermicular filaments (C_V), which decompose at ~590 °C; and (4) graphitic crystalline platelets (C_C), which decompose at ~800 °C [61–63]. The two dominant events observed for the $Ni_{10}P2$

catalyst suggested that the coke was predominantly composed of non-poisoning Cα and amorphous Cβ carbon species. In a more detailed analysis, the DTA results showed that the first event consisted of two steps, endothermic and exothermic (Fig. S9). The decomposition of hydroxides is endothermic, suggesting the formation of some amount of $Mg(OH)_2$ on the surface of the catalyst, while the exothermic peak is associated with the decomposition of Cα [64,65]. A small quantity of poisoning C_C coke was also detected for $Ni_{10}P0$. The presence of less poisoning coke was detected for $Ni_{10}P2$, probably due to the stronger basic sites, which decreased the rate of oligomeric carbon formation on the surface, due to increased water adsorption and greater gasification of carbonaceous compounds [18].

The basic sites of the support, acting together with the metallic sites, are responsible for the dehydrogenation of ethanol to acetaldehyde, which is the first stage of the ethanol vapor reforming reaction [17]. This occurs because the ethanol adsorbs dissociatively at the basic sites on the support surface. Subsequently, the ethoxy species is dehydrogenated to acetaldehyde by the metal site. Dehydrogenation continues until the formation of CH_x (when incomplete) or CO_2 (when complete). Additionally, the alkali metal oxides can decrease the formation of oligomeric carbon on the catalyst surface, due to high water adsorption, promoting the gasification of carbonaceous compounds [18]. Therefore, in agreement with the results observed for catalyst stability and coke formation, the CO_2 temperature-programmed desorption analyses (TPD-CO_2) showed increased basicity and a shift to higher temperatures for the catalysts prepared with Pluronic (Fig. 8c, Table 4). The $Ni_{10}P0$ catalyst presented a broad peak at 170 ºC, with total CO_2 desorption of 121 μmol/g. The amount of desorbed CO_2 increased for $Ni_{10}P2$ (167 μmol/g), with the peak position being shifted to a higher temperature of 240 °C. The smaller crystallite size and higher specific area resulted in a more defective

structure for $Ni_{10}P2$, with defects on the surface of the magnesium oxide favoring greater strength of the basic sites, because edges, corners, and twists provide O^{2-} sites with low coordination numbers [22]. The benefits of the greater basicity and the strength of the basic sites were reflected in the higher stability and lower poisoning by coke for the $Ni_{10}P2$ catalyst.

In an attempt to identify other possible effects leading to deactivation, such as sintering of the active phase, the spent catalysts were characterized by TEM (Fig. S10), which revealed particle size distributions similar to those obtained for the fresh catalysts (Fig. 5). Hence, sintering events were ruled out and the observed deactivation could be mainly attributed to the formation of coke. Additionally, the SEM images (Fig. 9) revealed differences in the carbon formed on the surfaces of the spent catalysts. The $Ni_{01}P0$ catalyst (Fig. 9b) had a small amount of vermicular carbon on the surface, which was much less than on the $Ni_{10}P0$ catalyst (Fig. 9d). On the other hand, the $Ni_{10}P2$ catalyst (Fig. 9f) presented no vermicular carbon, in agreement with the TG results. Hence, comparison of the $Ni_{01}P0$ and $Ni_{10}P0$ samples showed that consideration of particle size was important for decreasing the amount of vermicular carbon formed. Nonetheless, the textural characteristics obtained from the P2 support was also a driving force for decreasing the formation of structurally organized carbon deposits, which are recognized as being detrimental to catalytic activity by encapsulating the active sites. Some studies have suggested the possibility of amorphous carbon deposits also being responsible for deactivation [66,67]. However, the lower total amount of coke produced in the presence of small particles is a general factor for the maintenance of catalytic activity [68].

Table S4 shows the catalytic activities reported in the literature for some catalysts with similar compositions to those studied in this work. Comparison of the

catalysts is not straightforward, because there are many variations in the reaction parameters, such as temperature and reactant flow. For this reason, some catalysts can present stability during many hours or days [69], while for other catalysts, the activity drops in a few minutes [70]. Nonetheless, the fast and simple sol-gel synthesis presented in this study allowed the preparation of catalysts with high activity comparable to that of more complex catalysts or even to those employing noble metals as the active phase [71,72].

4. Conclusions

This study showed the benefits of dispersion of nickel in nanocrystalline magnesium oxides prepared for the ethanol steam reforming reaction. The structure-directing effect of the Pluronic P123 surfactant enabled the crystallite size to be decreased from 54 to 18 nm, favoring the dissolution of nickel atoms in the MgO lattice. The decrease of the MgO crystallite size led to increases of the pore volume and surface area. *In situ* XRD and XAS analyses evidenced that a low nickel loading and a small MgO crystallite size favored the dominant formation of NiMgO solid solution, which led to better dispersion of the metallic nickel particles formed during a reductive thermal activation process.

The effect of the size of the metallic particles on the catalytic conversion was enhanced by the textural properties of the catalyst prepared with Pluronic P123 surfactant. In the case of the same nickel loading, it was observed that for the lowest reaction temperature studied (400 °C) the $Ni_{10}P0$ sample converted 20% of the ethanol. In contrast, the catalysts prepared with surfactant ($Ni_{10}P1$ and $Ni_{10}P2$) converted 90%.

In the stability tests, catalyst deactivation decreased from 47% for $Ni_{10}P0$ to 7% for $Ni_{10}P2$. Reduced coke formation, as well as the change from poisoning Cv coke

(vermicular filaments) to less harmful monoatomic Cα coke, was found for the samples prepared with surfactant. These results were consistent with greater CO_2 chemisorption, while the desorption peak shifted to a higher temperature, suggesting formation of the strongest basic sites for the $Ni_{10}P2$ catalyst.

5. Acknowledgements

Financial support for this work was provided by the São Paulo State Research Foundation (FAPESP, grants #2014/11952-5, #2016/12752-5, and #2018/01258-5) and the Brazilian National Council for Scientific and Technological Development (CNPq). The authors are grateful to the Brazilian Synchrotron Light Laboratory (LNLS) in Campinas for use of the XPD beamline (proposal XPD-20170119) and the DXAS beamline (where the initial XAS experiments were performed) (proposal DXAS-20180409). Synchrotron SOLEIL provided access to the ROCK beamline (proposal #20191749), which was supported by a public grant overseen by the French National Research Agency (ANR) as part of the "*Investissements d'Avenir*" program (reference: ANR-10-EQPX-45).

6. References

[1] N. Kittner, F. Lill, D.M. Kammen, Energy storage deployment and innovation for the clean energy transition, Nat. Energy. 2 (2017) 17125. doi:10.1038/nenergy.2017.125.

[2] L.H. Vieira, L.G. Possato, T.F. Chaves, S.H. Pulcinelli, C. V. Santilli, L. Martins, Studies on dispersion and reactivity of vanadium oxides deposited on lamellar ferrierite zeolites for condensation of glycerol into bulky products, Mol. Catal. 458 (2018) 161–170. doi:10.1016/j.mcat.2017.11.027.

[3] L.G. Possato, M.D. Acevedo, C.L. Padró, V. Briois, A.R. Passos, S.H. Pulcinelli, C. V. Santilli, L. Martins, Activation of Mo and V oxides supported on ZSM-5 zeolite catalysts followed by in situ XAS and XRD and their uses in oxydehydration of glycerol, Mol. Catal. 481 (2020) 110158. doi:10.1016/j.mcat.2018.07.029.

[4] W.H. Cassinelli, L. Martins, M. Magnani, S.H. Pulcinelli, V. Briois, C. V Santilli, Time-resolved XAS/MS/Raman monitoring of mutual copper self-reduction and ethanol dehydrogenation reactions, RSC Adv. 6 (2016) 20453–20457. doi:10.1039/c5ra27403f.

[5] S. Weitemeyer, D. Kleinhans, T. Vogt, C. Agert, Integration of Renewable Energy

Sources in future power systems: The role of storage, Renew. Energy. 75 (2015) 14–20. doi:10.1016/j.renene.2014.09.028.
[6] S.M.M. Ehteshami, S.H. Chan, The role of hydrogen and fuel cells to store renewable energy in the future energy network - potentials and challenges, Energy Policy. 73 (2014) 103–109. doi:10.1016/j.enpol.2014.04.046.
[7] E. Csefalvay, G.R. Akien, L. Qi, I.T. Horvath, Definition and application of ethanol equivalent: Sustainability performance metrics for biomass conversion to carbon-based fuels and chemicals, Catal. Today. 239 (2015) 50–55. doi:10.1016/j.cattod.2014.02.006.
[8] M. Ni, D.Y.C. Leung, M.K.H. Leung, A review on reforming bio-ethanol for hydrogen production, Int. J. Hydrogen Energy. 32 (2007) 3238–3247. doi:10.1016/j.ijhydene.2007.04.038.
[9] V. Nichele, M. Signoretto, F. Pinna, F. Menegazzo, I. Rossetti, G. Cruciani, G. Cerrato, A. Di Michele, Ni/ZrO_2 catalysts in ethanol steam reforming: Inhibition of coke formation by CaO-doping, Appl. Catal. B Environ. 150–151 (2014) 12–20. doi:10.1016/j.apcatb.2013.11.037.
[10] P. Osorio-Vargas, N.A. Flores-Gonzalez, R.M. Navarro, J.L.G. Fierro, C.H. Campos, P. Reyes, Improved stability of Ni/Al_2O_3 catalysts by effect of promoters (La_2O_3, CeO_2) for ethanol steam-reforming reaction, Catal. Today. 259 (2016) 27–38. doi:10.1016/j.cattod.2015.04.037.
[11] I.A. Carbajal-Ramos, M.F. Gomez, A.M. Condo, S. Bengio, J.J. Andrade-Gamboa, M.C. Abello, F.C. Gennari, Catalytic behavior of Ru supported on $Ce_{0.8}Zr_{0.2}O_2$ for hydrogen production, Appl. Catal. B-Environmental. 181 (2016) 58–70. doi:10.1016/j.apcatb.2015.07.025.
[12] V. V Thyssen, T.A. Maia, E.M. Assaf, Cu and Ni catalysts supported on gamma-Al_2O_3 and SiO_2 assessed in glycerol steam reforming reaction, J. Braz. Chem. Soc. 26 (2015) 22–31. doi:10.5935/0103-5053.20140209.
[13] T.A. Maia, J.D.A. Bellido, E.M. Assaf, J.M. Assaf, Hydrogen production by ethanol steam reforming using Cu/Ni/gamma-Al_2O_3 catalysts, Quim. Nova. 30 (2007) 339–345. doi:10.1590/s0100-40422007000200019.
[14] F.L.S. Carvalho, Y.J.O. Asencios, J.D.A. Bellido, E.M. Assaf, Bio-ethanol steam reforming for hydrogen production over Co_3O_4/CeO_2 catalysts synthesized by one-step polymerization method, Fuel Process. Technol. 142 (2016) 182–191. doi:10.1016/j.fuproc.2015.10.010.
[15] W.H. Cassinelli, L. Martins, A.R. Passos, S.H. Pulcinelli, A. Rochet, V. Briois, C. V Santilli, Correlation between structural and catalytic properties of copper supported on porous alumina for the ethanol dehydrogenation reaction, ChemCatChem. 7 (2015) 1668–1677. doi:10.1002/cctc.201500112.
[16] L.G. Possato, E. Pereira, R.G.L. Gonçalves, S.H. Pulcinelli, L. Martins, C. V. Santilli, Controlling the porosity and crystallinity of MgO catalysts by addition of surfactant in the sol-gel synthesis, Catal. Today. 344 (2020) 52–58. doi:10.1016/j.cattod.2018.10.027.
[17] D.K. Liguras, D.I. Kondarides, X.E. Verykios, Production of hydrogen for fuel cells by steam reforming of ethanol over supported noble metal catalysts, Appl. Catal. B-Environmental. 43 (2003) 345–354. doi:10.1016/s0926-3373(02)00327-2.
[18] D.L. Trimm, Catalysts for the control of coking during steam reforming, Catal. Today. 49 (1999) 3–10. doi:10.1016/s0920-5861(98)00401-5.
[19] R. Zanganeh, M. Rezaei, A. Zamaniyan, Dry reforming of methane to synthesis gas on NiO-MgO nanocrystalline solid solution catalysts, Int. J. Hydrogen Energy. 37(7) (2013) 3012–3018. doi:10.1016/j.ijhydene.2012.12.089.
[20] F. Meshkani, M. Rezaei, Nickel catalyst supported on magnesium oxide with high

surface area and plate-like shape: A highly stable and active catalyst in methane reforming with carbon dioxide, Catal. Commun. 12(11) (2011) 1046–1050. doi:10.1016/j.catcom.2011.03.013.
[21] M. Rezaei, M. Khajenoori, B. Nematollahi, Synthesis of high surface area nanocrystalline MgO by pluronic P123 triblock copolymer surfactant, Powder Technol. 205 (2011) 112–116. doi:10.1016/j.powtec.2010.09.001.
[22] M.J. Climent, A. Corma, S. Iborra, M. Mifsud, MgO nanoparticle-based multifunctional catalysts in the cascade reaction allows the green synthesis of anti-inflammatory agents, J. Catal. 247 (2007) 223–230. doi:10.1016/j.jcat.2007.02.003.
[23] F. Meshkani, M. Rezaei, Nanocrystalline MgO supported nickel-based bimetallic catalysts for carbon dioxide reforming of methane, Int. J. Hydrogen Energy. (2010). doi:10.1016/j.ijhydene.2010.07.138.
[24] H. Canova, A. Fontoura, R.T. Neuenschwander, B. Diaz, C.B. Rodella, Upgrades to the XRD1 beamline optics and endstation at the LNLS, in: J. Phys. Conf. Ser., IOP Publishing, n.d.: p. 12004.
[25] L.G. Possato, W.H. Cassinelli, C.I. Meyer, T. Garetto, S.H. Pulcinelli, C. V. Santilli, L. Martins, Thermal treatments of precursors of molybdenum and vanadium oxides and the formed MoxVyOz phases active in the oxydehydration of glycerol, Appl. Catal. A Gen. 532 (2017) 1–11. doi:10.1016/j.apcata.2016.12.010.
[26] H.M. Rietveld, A profile refinement method for nuclear and magnetic structures, J. Appl. Crystallogr. 2 (1969) 65–71. doi:10.1107/S0021889869006558.
[27] L. Lutterotti, S. Matthies, H.R. Wenk, MAUD: a friendly Java program for Material Analysis Using Diffraction, Univ. Degli Stud. Di Trento Univ. Calif. Berkeley. 21 (1999) 14–15. doi:DOI 10.1016/j.bmcl.2007.03.093.
[28] V. Briois, C. La Fontaine, S. Belin, L. Barthe, T. Moreno, V. Pinty, A. Carcy, R. Girardot, E. Fonda, ROCK: The new Quick-EXAFS beamline at SOLEIL, J. Phys. Conf. Ser., 712 (2016) 012149. doi:10.1088/1742-6596/712/1/012149.
[29] C. Lesage, E. Devers, C. Legens, G. Fernandes, O. Roudenko, V. Briois, High pressure cell for edge jumping X-ray absorption spectroscopy: Applications to industrial liquid sulfidation of hydrotreatment catalysts, Catal. Today. 336 (2019) 63–73. doi:10.1016/j.cattod.2019.01.081.
[30] C. La Fontaine, L. Barthe, A. Rochet, V. Briois, X-ray absorption spectroscopy and heterogeneous catalysis: Performances at the SOLEIL's SAMBA beamline, Catal. Today. 205 (2013) 148–158. doi:10.1016/j.cattod.2012.09.032.
[31] B. Ravel, M. Newville, ATHENA, ARTEMIS, HEPHAESTUS: data analysis for X-ray absorption spectroscopy using IFEFFIT, J. Synchrotron Radiat. 12 (2005) 537–541. doi:10.1107/s0909049505012719.
[32] Z. Zhang, W. Hu, S. Xiao, Melting, melting competition, and structural transitions between shell-closed icosahedral and octahedral nickel nanoclusters, Phys. Rev. B - Condens. Matter Mater. Phys. 73 (2006) 125443. doi:10.1103/PhysRevB.73.125443.
[33] A. Frenkel, Solving the 3D structure of metal nanoparticles, Zeitschrift Fur Krist. 222 (2007) 605–611. doi:10.1524/zkri.2007.222.11.605.
[34] J.M. Montejano-Carrizales, F. Aguilera-Granja, J.L. Morán-López, Direct enumeration of the geometrical characteristics of clusters, Nanostructured Mater. 3 (1997) 269–287. doi:10.1016/S0965-9773(97)00168-2.
[35] S. Hanukovich, A. Dang, P. Christopher, Influence of metal oxide support acid sites on Cu-catalyzed nonoxidative dehydrogenation of ethanol to acetaldehyde, ACS Catal. 9 (2019) 3537–3550. doi:10.1021/acscatal.8b05075.
[36] G. Bergeret, P. Gallezot, Particle size and dispersion measurements, in: Handb. Heterog. Catal., 2008: p. 740. doi:10.1002/9783527610044.hetcat0038.

[37] A.G. Sato, D.P. Volanti, D.M. Meira, S. Damyanova, E. Longo, J.M.C. Bueno, Effect of the ZrO_2 phase on the structure and behavior of supported Cu catalysts for ethanol conversion, J. Catal. 307 (2013) 1–17. doi:10.1016/j.jcat.2013.06.022.
[38] S. Brunauer, P.H. Emmett, E. Teller, Adsorption of gases in multimolecular layers, J. Am. Chem. Soc. 60 (1938) 309–319. doi:10.1021/ja01269a023.
[39] E.P. Barrett, L.G. Joyner, P.P. Halenda, The determination of pore volume and area distributions in porous substances. I. Computations from nitrogen isotherms, J. Am. Chem. Soc. 73(1) (1951) 373–380. doi:10.1021/ja01145a126.
[40] D.A.G. Pérez, A.M. Jorge, C.S. Kiminami, C. Bolfarini, W.J. Botta, Ultrafine-grained Ti-13Nb-13Zr alloy produced by severe plastic deformation, in: Mater. Res., 20(2) (2017) 404–410. doi:10.1590/1980-5373-mr-2017-0037.
[41] A.R. Passos, L. Martins, S.H. Pulcinelli, C. V Santilli, V. Briois, Effect of the balance between Co(II) and Co(0) oxidation states on the catalytic activity of cobalt catalysts for ethanol steam reforming, Catal. Today. 229 (2014) 88–94. doi:10.1016/j.cattod.2013.10.080.
[42] W. Gerlach, Die Gitterstruktur der Erdalkalioxyde, Zeitschrift für Phys. 9 (1922) 184–192. doi:10.1007/BF01326966.
[43] G.T. Wurzler, R.C. Rabelo-Neto, L. V. Mattos, M.A. Fraga, F.B. Noronha, Steam reforming of ethanol for hydrogen production over MgO-supported Ni-based catalysts, Appl. Catal. A Gen. 518 (2016) 115–128. doi:10.1016/j.apcata.2015.11.020.
[44] P. Scherrer, Bestimmung der Größe und der inneren Struktur von Kolloidteilchen mittels Röntgenstrahlen, Nachrichten von Der Gesellschaft Der Wissenschaften Zu Göttingen, Math. Klasse. (1918).
[45] Y.-H. Wang, H.-M. Liu, B.-Q. Xu, Durable Ni/MgO catalysts for CO_2 reforming of methane: Activity and metal-support interaction, J. Mol. Catal. A Chem. 299 (2009) 44–52. doi:10.1016/j.molcata.2008.09.025.
[46] IUPAC, Reporting physisorption data for gas/solid systems, Pure Appl. Chem. 54 (1982) 1–18. doi:10.1351/pac198557040603.
[47] Z.A. Alothman, A review: Fundamental aspects of silicate mesoporous materials, Materials (Basel). 5 (2012) 2874–2902. doi:10.3390/ma5122874.
[48] J. Green, Calcination of precipitated $Mg(OH)_2$ to active MgO in the production of refractory and chemical grade MgO, J. Mater. Sci. 18 (1983) 637–651. doi:10.1007/BF00745561.
[49] M. Rezaei, M. Khajenoori, B. Nematollahi, Preparation of nanocrystalline MgO by surfactant assisted precipitation method, Mater. Res. Bull. 10 (2011) 1632–1637. doi:10.1016/j.materresbull.2011.06.007.
[50] T. Ohkubo, T. Ogura, H. Sakai, M. Abe, Synthesis of highly-ordered mesoporous silica particles using mixed cationic and anionic surfactants as templates, J. Colloid Interface Sci. 312(1) (2007) 42–46. doi:10.1016/j.jcis.2007.02.043.
[51] D. Müter, T. Shin, B. Demé, P. Fratzl, O. Paris, G.H. Findenegg, Surfactant self-assembly in cylindrical silica nanopores, J. Phys. Chem. Lett. 1(9) (2010) 1442–1446. doi:10.1021/jz100279y.
[52] M. Shahid, J.L. Liu, Z. Ali, I. Shakir, M.F. Warsi, Structural and electrochemical properties of single crystalline MoV_2O_8 nanowires for energy storage devices, J. Power Sources. 230 (2013) 277–281. doi:10.1016/j.jpowsour.2012.12.033.
[53] R. Zanganeh, M. Rezaei, A. Zamaniyan, Preparation of nanocrystalline NiO-MgO solid solution powders as catalyst for methane reforming with carbon dioxide: Effect of preparation conditions, Adv. Powder Technol. 3 (2014) 1111–1117. doi:10.1016/j.apt.2014.02.015.
[54] Y. Wang, T. Ji, X. Yang, Y. Wang, Comparative Study on Steam Reforming of

Single-and Multicomponent Model Compounds of Biomass Fermentation for Producing Biohydrogen over Mesoporous Ni/MgO Catalyst, Enery Fuels, 30(10) (2016) 8432–8440. doi:10.1021/acs.energyfuels.6b02130.
[55] Y. Yan, Y. Dai, H. He, Y. Yu, Y. Yang, A novel W-doped Ni-Mg mixed oxide catalyst for CO_2 methanation, Appl. Catal. B Environ. 196 (2016) 108–116. doi:10.1016/j.apcatb.2016.05.016.
[56] Y.J.O. Asencios, P.A.P. Nascente, E.M. Assaf, Partial oxidation of methane on NiO–MgO–ZrO_2 catalysts, Fuel. 97 (2012) 630–637. doi:10.1016/j.fuel.2012.02.067.
[57] F. Aupretre, C. Descorme, D. Duprez, Bio-ethanol catalytic steam reforming over supported metal catalysts, Catal. Commun. 3 (2002) 263–267. doi:10.1016/s1566-7367(02)00118-8.
[58] E.Y. Garcia, M.A. Laborde, hydrogen-production by the steam reforming of ethanol - thermodynamic analysis, Int. J. Hydrogen Energy. 16 (1991) 307–312. doi:10.1016/0360-3199(91)90166-g.
[59] K. Vasudeva, N. Mitra, P. Umasankar, S.C. Dhingra, Steam reforming of ethanol for hydrogen production: Thermodynamic analysis, Int. J. Hydrogen Energy. 21 (1996) 13–18. doi:10.1016/0360-3199(95)00030-h.
[60] A. Lopez Ortiz, R.B. Pallares Samano, M.J. Melendez Zaragoza, V. Collins-Martinez, Thermodynamic analysis and process simulation for the H_2 production by dry reforming of ethanol with $CaCO_3$, Int. J. Hydrogen Energy. 40 (2015) 17172–17179. doi:10.1016/j.ijhydene.2015.07.115.
[61] J. Vicente, J. Ereña, C. Montero, M.J. Azkoiti, J. Bilbao, A.G. Gayubo, Reaction pathway for ethanol steam reforming on a Ni/SiO_2 catalyst including coke formation, Int. J. Hydrogen Energy. 39(33) (2014) 18820–18834. doi:10.1016/j.ijhydene.2014.09.073.
[62] S. Mahamulkar, K. Yin, P.K. Agrawal, R.J. Davis, C.W. Jones, A. Malek, H. Shibata, Formation and oxidation/gasification of carbonaceous deposits: A Review, Ind. Eng. Chem. Res. 55(37) (2016) 9760–9818. doi:10.1021/acs.iecr.6b02220.
[63] J. Guo, H. Lou, X. Zheng, The deposition of coke from methane on a Ni/$MgAl_2O_4$ catalyst, Carbon. 45(6) (2007) 1314–1321. doi:10.1016/j.carbon.2007.01.011.
[64] A.G. Bannov, M. V. Popov, P.B. Kurmashov, Thermal analysis of carbon nanomaterials: advantages and problems of interpretation, J. Therm. Anal. Calorim. 142 (2020) 349–370. doi:10.1007/s10973-020-09647-2.
[65] M.A. Alavi, A. Morsali, Syntheses and characterization of $Mg(OH)_2$ and MgO nanostructures by ultrasonic method, Ultrason. Sonochem. 17 (2010) 441–446. doi:10.1016/j.ultsonch.2009.08.013.
[66] C. Montero, A. Remiro, B. Valle, L. Oar-Arteta, J. Bilbao, A.G. Gayubo, Origin and nature of coke in ethanol steam reforming and its role in deactivation of Ni/La_2O_3-αAl_2O_3 Catalyst, Ind. Eng. Chem. Res. 58 (2019) 14736–14751. doi:10.1021/acs.iecr.9b02880.
[67] H.S. Bengaard, J.K. Nørskov, J. Sehested, B.S. Clausen, L.P. Nielsen, A.M. Molenbroek, J.R. Rostrup-Nielsen, Steam reforming and graphite formation on Ni catalysts, J. Catal. 25 (2002) 365–384. doi:10.1006/jcat.2002.3579.
[68] A.R. Passos, C. La Fontaine, S.H. Pulcinelli, C.V. Santilli, V. Briois, Quick-EXAFS and Raman monitoring of activation, reaction and deactivation of NiCu catalysts obtained from hydrotalcite-like precursors, Phys. Chem. Chem. Phys. 22 (2020) 18835–18848. doi:10.1039/d0cp00380h.
[69] J.A. Santander, G.M. Tonetto, M.N. Pedernera, E. López, Ni/CeO_2–MgO catalysts supported on stainless steel plates for ethanol steam reforming, Int. J. Hydrogen Energy. 42 (2017) 9482–9492. doi:10.1016/j.ijhydene.2017.03.169.

[70] L. Santamaria, M. Artetxe, G. Lopez, M. Cortazar, M. Amutio, J. Bilbao, M. Olazar, Effect of CeO_2 and MgO promoters on the performance of a Ni/Al_2O_3 catalyst in the steam reforming of biomass pyrolysis volatiles, Fuel Process. Technol. 198 (2020) 106223. doi:10.1016/j.fuproc.2019.106223.
[71] F. Frusteri, S. Freni, L. Spadaro, V. Chiodo, G. Bonura, S. Donato, S. Cavallaro, H_2 production for MC fuel cell by steam reforming of ethanol over MgO supported Pd, Rh, Ni and Co catalysts, Catal. Commun. 5 (2004) 611–615. doi:10.1016/j.catcom.2004.07.015.
[72] A. Erdohelyi, J. Raskó, T. Kecskés, M. Tóth, M. Dömök, K. Baán, Hydrogen formation in ethanol reforming on supported noble metal catalysts, Catal. Today. 116 (2006) 367–376. doi:10.1016/j.cattod.2006.05.073.
[73] F. Frusteri, S. Freni, V. Chiodo, L. Spadaro, O. Di Blasi, G. Bonura, S. Cavallaro, Steam reforming of bio-ethanol on alkali-doped Ni/MgO catalysts: Hydrogen production for MC fuel cell, Appl. Catal. A Gen. 270 (2004) 1–7. doi:10.1016/j.apcata.2004.03.052.
[74] S. Sang, Z.J. Zhao, H. Tian, Z. Sun, H. Li, S. Assabumrungrat, T. Muhammad, L. Zeng, J. Gong, Promotional role of MgO on sorption-enhanced steam reforming of ethanol over Ni/CaO catalysts, AIChE J. 66(4) (2019) 16877. doi:10.1002/aic.16877.
[75] A.J. Vizcaíno, A. Carrero, J.A. Calles, Comparison of ethanol steam reforming using Co and Ni catalysts supported on SBA-15 modified by Ca and Mg, Fuel Process. Technol. 146 (2016) 99–109. doi:10.1016/j.fuproc.2016.02.020.

Table 1. Crystallite sizes and cell parameters of the MgO cubic structure (XRD data), and percentages of NiMgO and NiO (XANES data) in the calcined samples.

Sample	Average crystallite size of MgO (nm)	Cell parameter of unloaded MgO (nm)	Cell parameter of loaded MgO (nm)	NiMgO (%)	NiO (%)
$Ni_{01}P0$	53	0.42202	0.42326	100	0
$Ni_{10}P0$	54	0.42202	0.42301	70	30
$Ni_{10}P1$	25	0.42213	0.42270	90	10
$Ni_{10}P2$	18	0.42261	0.42265	93	7

Table 2. Textural properties and nickel contents (wt.%) determined by EDX.

Sample	S_{BET} (m^2/g)	V_{meso} (cm^3/g)	Mesopore size (nm)	Ni (wt.%)
$Ni_{01}P0$	47 (2)	0.25 (0.0)	22	2
$Ni_{10}P0$	21	0.16	30	11
$Ni_{10}P1$	57 (32)	0.50 (0.15)	40	9
$Ni_{10}P2$	50 (51)	0.35 (0.30)	33	13

The values in parentheses refer to unloaded MgO supports P0, P1, and P2.

Table 3. Hydrogen consumption, reducibility, and quantitative distribution of metallic nickel, as a function of temperature, obtained by TPR analysis.

Sample	H_2 cons. (μmol/g)	Reducibility (%)	25-400 °C (%)	400-700 °C (%)	700-1000 °C (%)
$Ni_{01}P0$	448	100	0	76	24
$Ni_{10}P0$	2100	100	9	42	49
$Ni_{10}P1$	840	55	5	33	62
$Ni_{10}P2$	1640	66	15	35	50

Table 4. Deactivation, TGA, and dTG results, and information about desorbed CO_2 during the TPD analysis.

Sample	Deactivation (%)	TGA (wt.%)	dTG peak (°C)	CO_2 (µmol/ g)	Peak CO_2 desorp. (°C)
$Ni_{10}P0$	47	16	515	121	170
$Ni_{10}P2$	7	9	340, 430	167	240

FIGURE CAPTIONS

Figure 1. (a) X-ray powder diffraction patterns for the calcined $Ni_{01}P0$, $Ni_{10}P0$, $Ni_{10}P1$, and $Ni_{10}P2$ samples, performed using a conventional diffractometer (Cu Kα radiation, ~8 keV). (b) X-ray absorption spectra in the XANES region for the Ni, NiO, and MgO standards and all the calcined samples.

Figure 2. Mesopore size distributions for the calcined samples.

Figure 3. *In situ* XRD measurements during thermal activation for (a) $Ni_{10}P0$ and (b) $Ni_{10}P2$. (c) Evolution of the normalized full width at half maximum (β/β_{max}) for the (220) plane during the activation.

Figure 4. Evolution of the concentration profiles of nickel components, as a function of activation temperature, determined from the XAS linear combination fits: (a) $Ni_{01}P0$, (b) $Ni_{10}P0$, (c) $Ni_{10}P1$, and (d) $Ni_{10}P2$.

Figure 5. (a) Mapping of nickel species performed by electron diffraction after reduction of the $Ni_{10}P0$ and $Ni_{10}P2$ samples, and (b) metallic nickel particle size distributions.

Figure 6. (a) Ethanol conversions during the ethanol steam reforming reaction at different temperatures, and product distributions during reaction for (b) $Ni_{10}P0$ and (c) $Ni_{10}P2$.

Figure 7. Fourier transformed and Fourier back-transformed EXAFS signals for (a, b) $Ni_{10}P0$ and (c, d) $Ni_{10}P2$, at 500 °C, during the ethanol steam reforming reaction.

Figure 8. (a) Isothermal stability test at 500 °C during the ethanol steam reforming reaction, using catalysts with the same metallic nickel concentration. (b) TGA and dTG curves for the spent catalysts after 6 h of reaction at 500 °C. (c) TPD-CO_2 profiles for the $Ni_{10}P0$ and $Ni_{10}P2$ samples.

Figure 9. SEM images at different magnifications for (a) (b) $Ni_{01}P0$, (c) (d) $Ni_{10}P0$, and (e) (f) $Ni_{10}P2$.

FIGURE 1

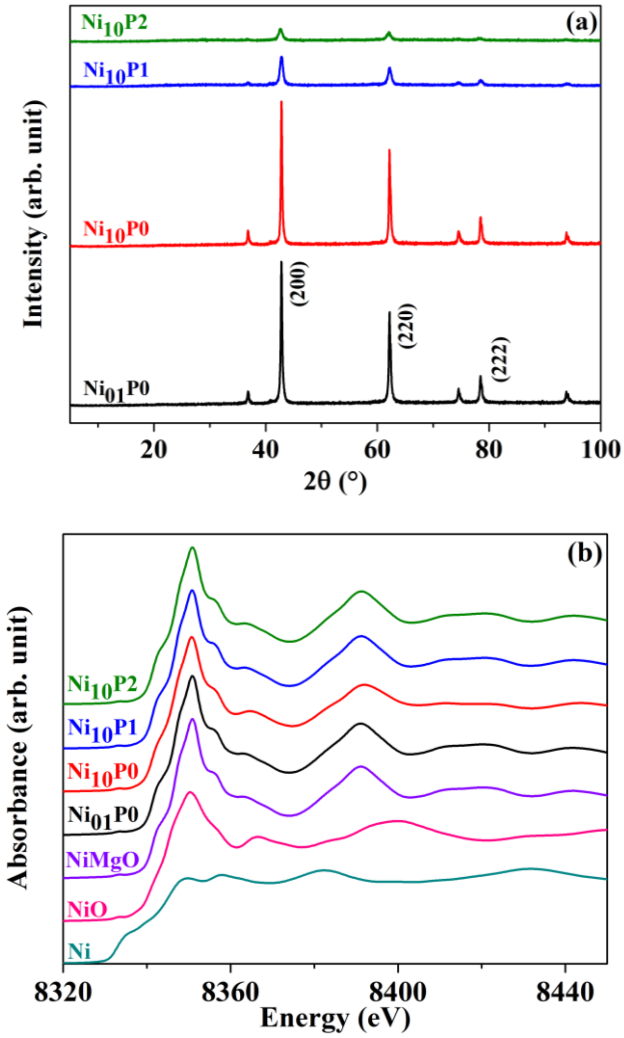
(a)
Ni10P2
Ni10P1
Ni10P0
Ni01P0
(200)
(220)
(222)
Intensity (arb. unit)
20
40
60
80
100
2θ (°)
(b)
Ni10P2
Ni10P1
Ni10P0
Ni01P0
NiMgO
NiO
Ni
Absorbance (arb. unit)
8320
8360
8400
8440
Energy (eV)

FIGURE 2

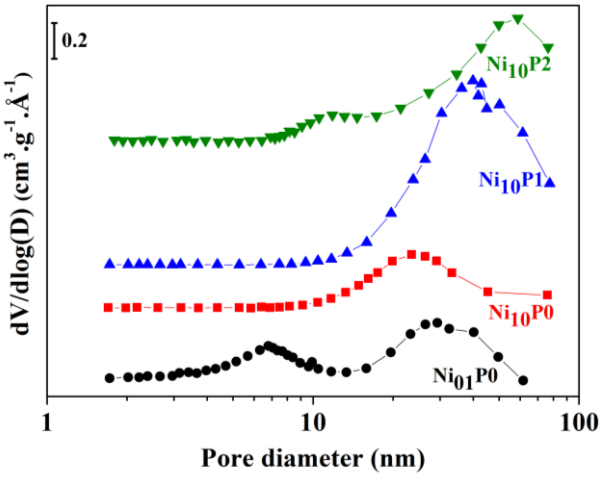
0.2
dV/dlog(D) (cm3.g-1.Å-1)
Ni10P2
Ni10P1
Ni10P0
Ni01P0
1
10
100
Pore diameter (nm)

FIGURE 3

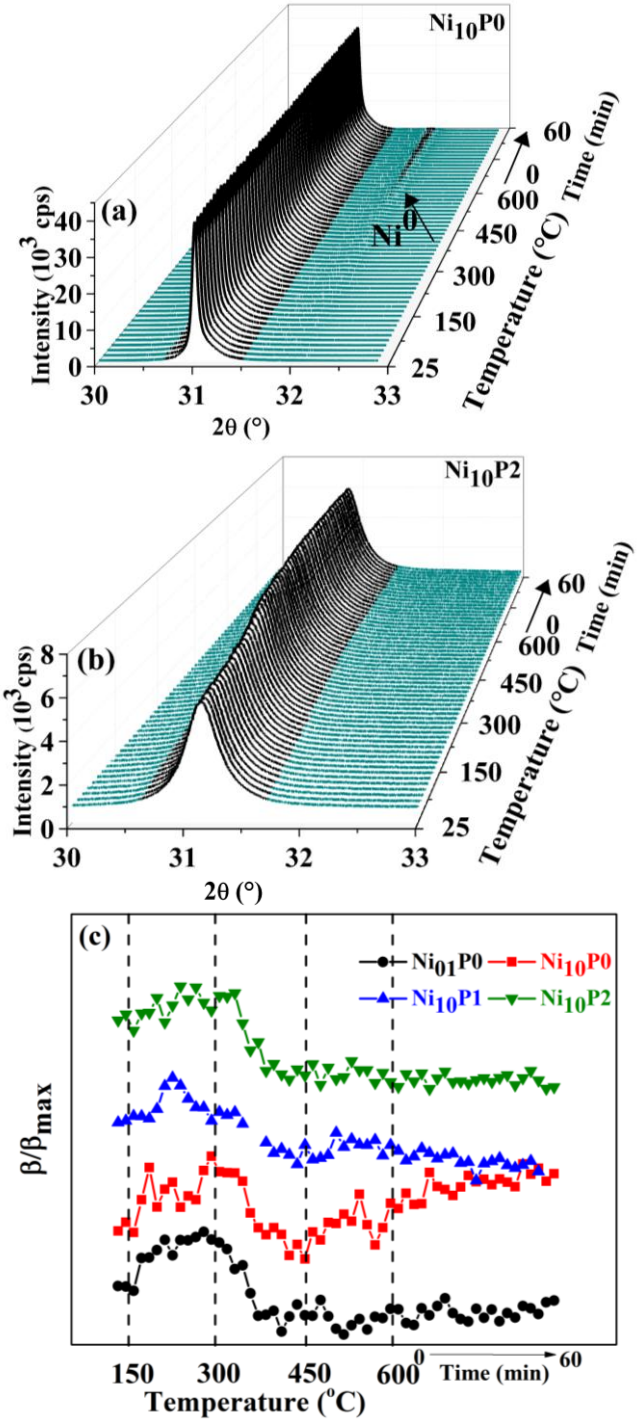
Ni10P0
(a)
Intensity (10^3 cps)
Ni 0
2θ (°)
Temperature (°C)
Time (min)
Ni10P2
(b)
(c)
Ni01P0
Ni10P0
Ni10P1
Ni10P2
β/βmax
Temperature (°C)
Time (min)

FIGURE 4

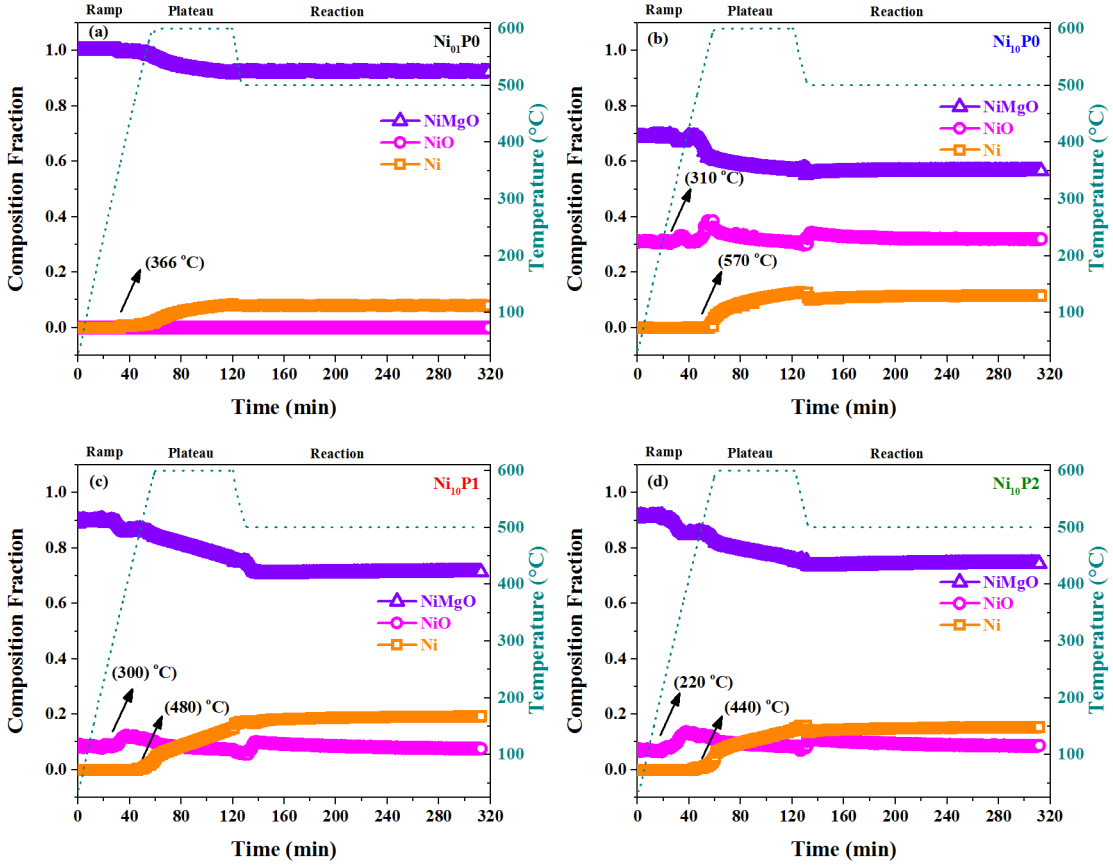
Ramp
Plateau
Reaction
(a)
Ni01P0
NiMgO
NiO
Ni
(366 °C)
Composition Fraction
Temperature (°C)
Time (min)
(b)
Ni10P0
(310 °C)
(570 °C)
(c)
Ni10P1
(300) °C)
(480) °C)
(d)
Ni10P2
(220 °C)
(440) °C)

FIGURE 5

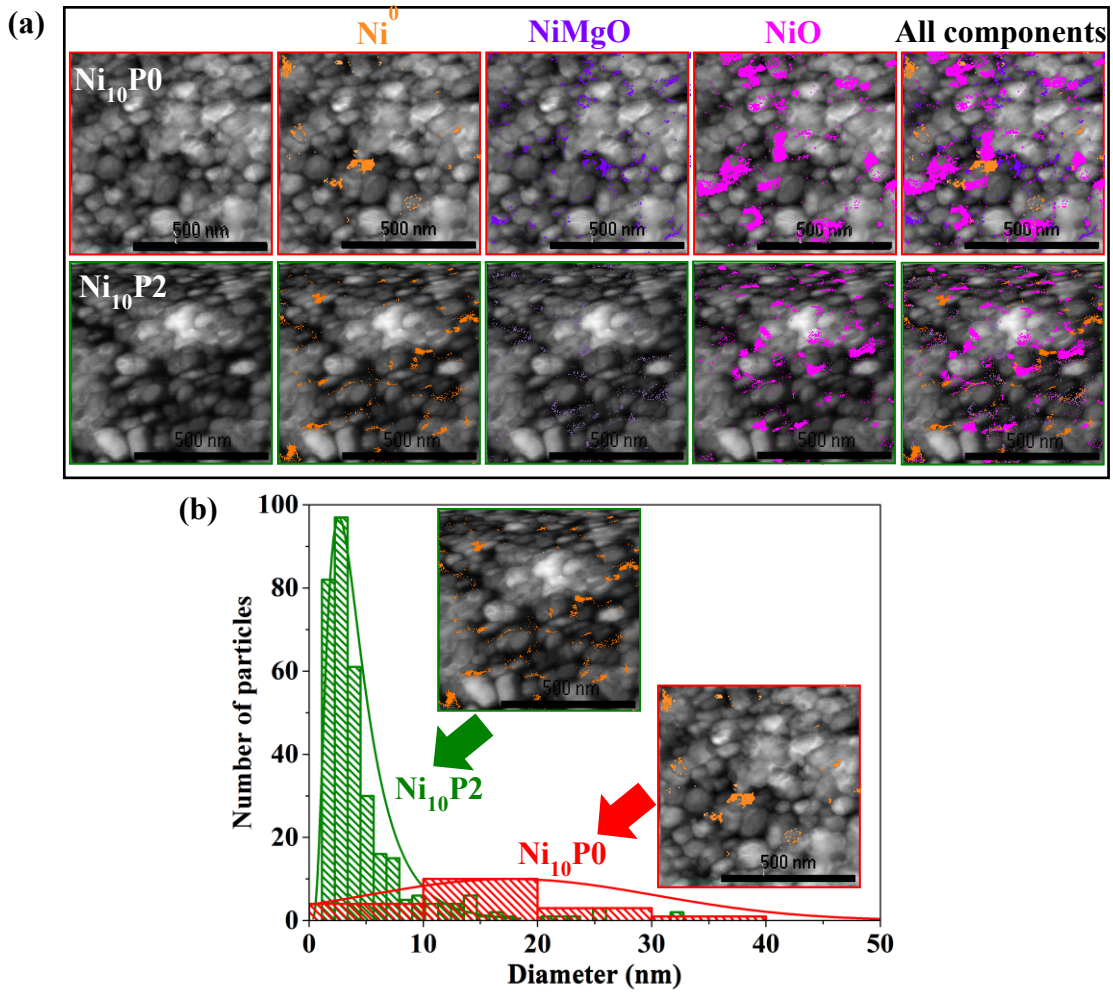
(a)
Ni0
NiMgO
NiO
All components
Ni10P0
Ni10P2
500 nm
(b)
Number of particles
Diameter (nm)
Ni10P2
Ni10P0
0
20
40
60
80
100
0
10
20
30
40
50

FIGURE 6

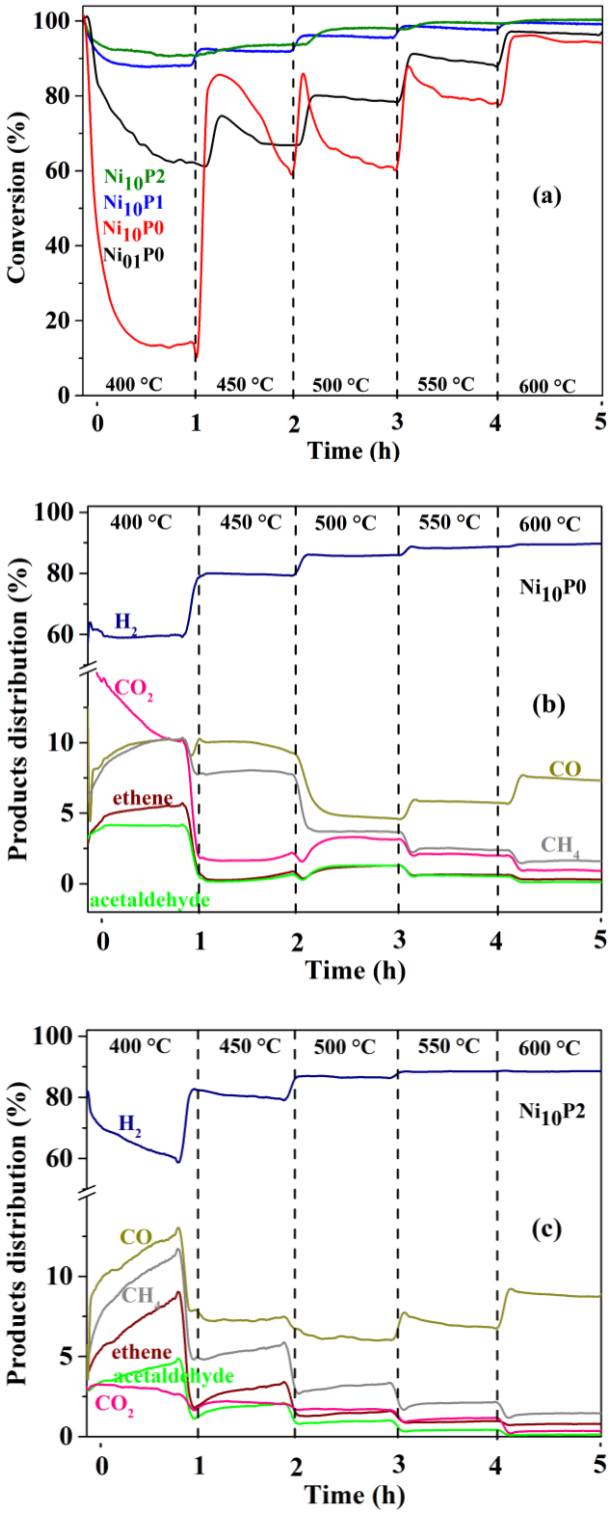
Conversion (%)
Time (h)
Ni10P2
Ni10P1
Ni10P0
Ni01P0
(a)
400 °C
450 °C
500 °C
550 °C
600 °C
Products distribution (%)
H2
CO2
ethene
acetaldehyde
CO
CH4
Ni10P0
(b)
Ni10P2
(c)

FIGURE 7

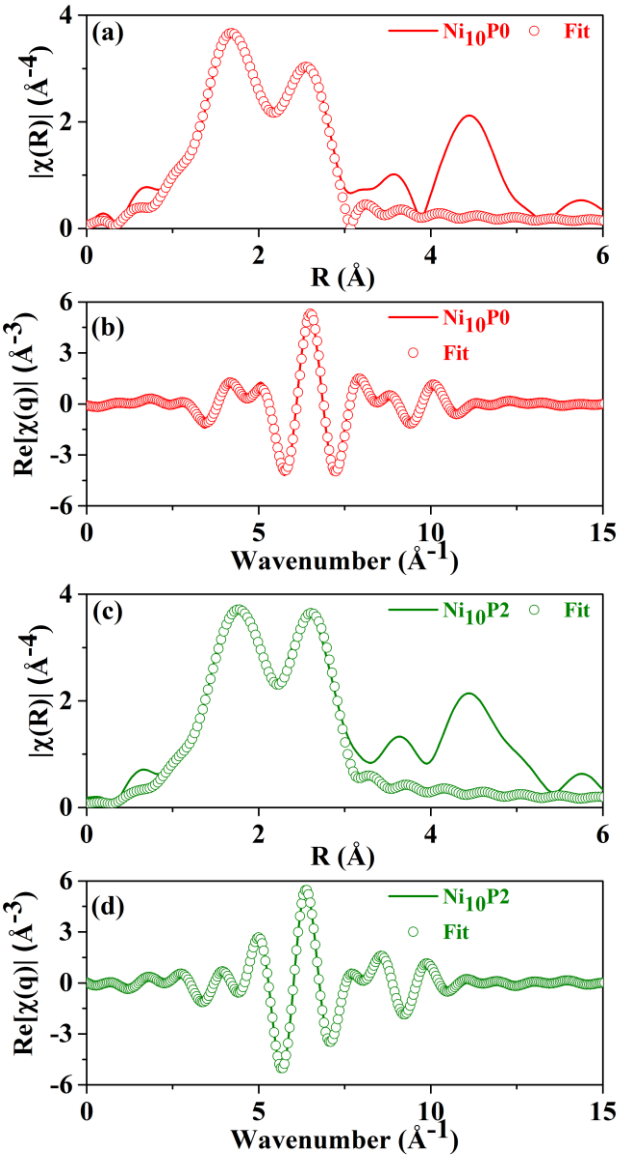
(a)
Ni10P0
Fit
|χ(R)| (Å-4)
R (Å)
(b)
Ni10P0
Fit
Re[χ(q)| (Å-3)
Wavenumber (Å-1)
(c)
Ni10P2
Fit
|χ(R)| (Å-4)
R (Å)
(d)
Ni10P2
Fit
Re[χ(q)| (Å-3)
Wavenumber (Å-1)

FIGURE 8

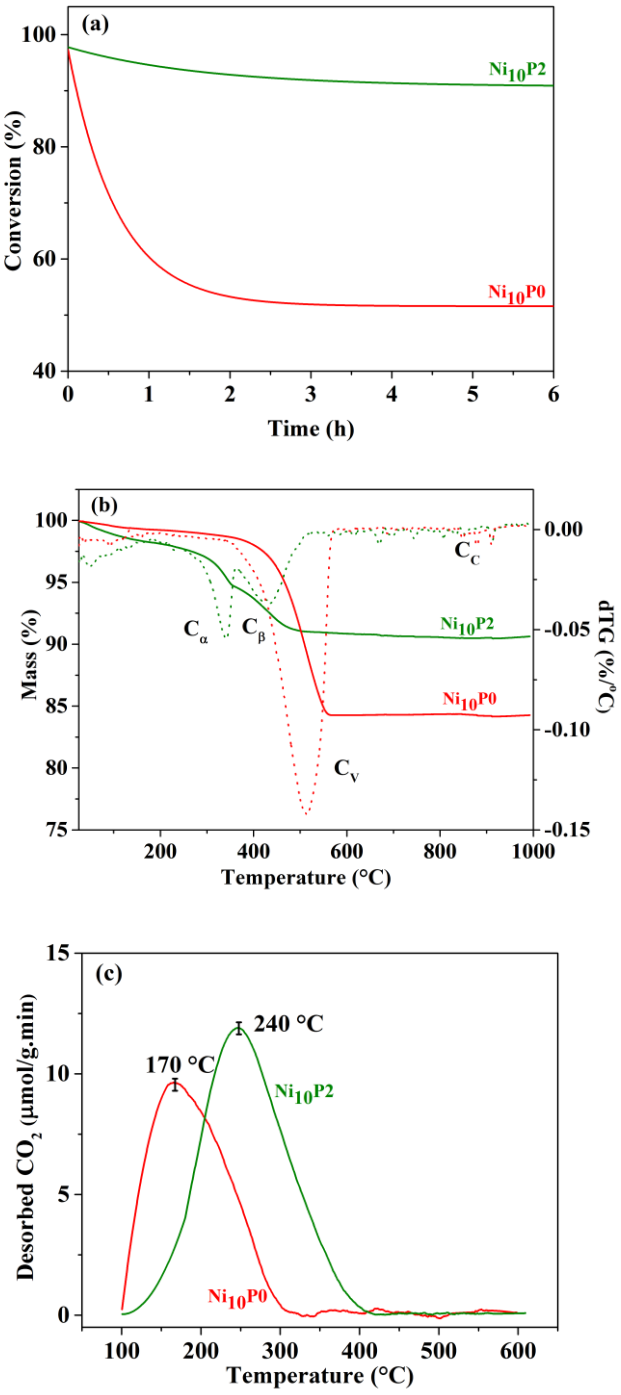
(a)
Conversion (%)
Time (h)
Ni10P2
Ni10P0
(b)
Mass (%)
dTG (%/°C)
Temperature (°C)
Cα
Cβ
Cγ
CV
Ni10P2
Ni10P0
(c)
Desorbed CO2 (μmol/g.min)
Temperature (°C)
170 °C
240 °C
Ni10P2
Ni10P0

FIGURE 9

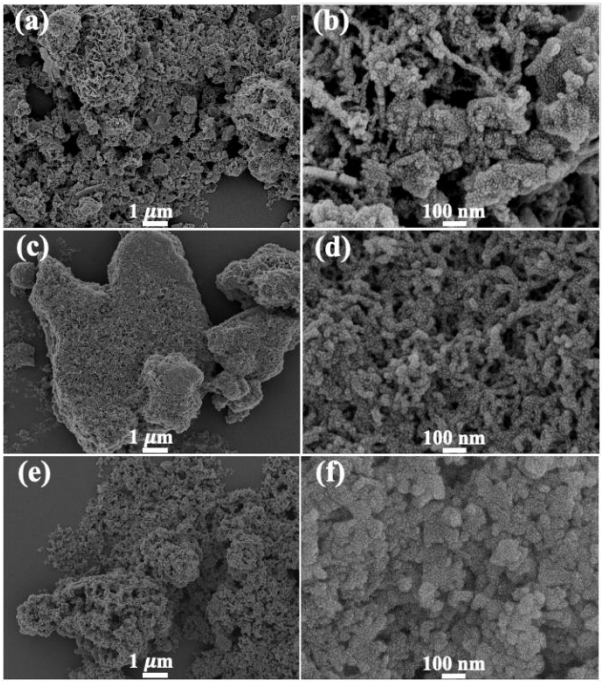

SUPPLEMENTARY MATERIAL

Sol-gel synthesis of nanocrystalline MgO and its application as support in Ni/MgO catalysts for ethanol steam reforming

Luiz G. Possato[a,b]*, Rosembergue G. L. Gonçalves[a], Rodrigo M. M. Santos[a], Thiago F. Chaves[a], Valérie Briois[b], Sandra H. Pulcinelli[a], Leandro Martins[a] and Celso V. Santilli[a]

[a] *Universidade Estadual Paulista (Unesp), Instituto de Química, Campus de Araraquara, Rua Prof. Francisco Degni 55, 14800-060 Araraquara, SP, Brazil*

[b] *Synchrotron SOLEIL, L'Orme des Merisiers, BP48, Saint Aubin, 91192 Gif-sur Yvette, France*

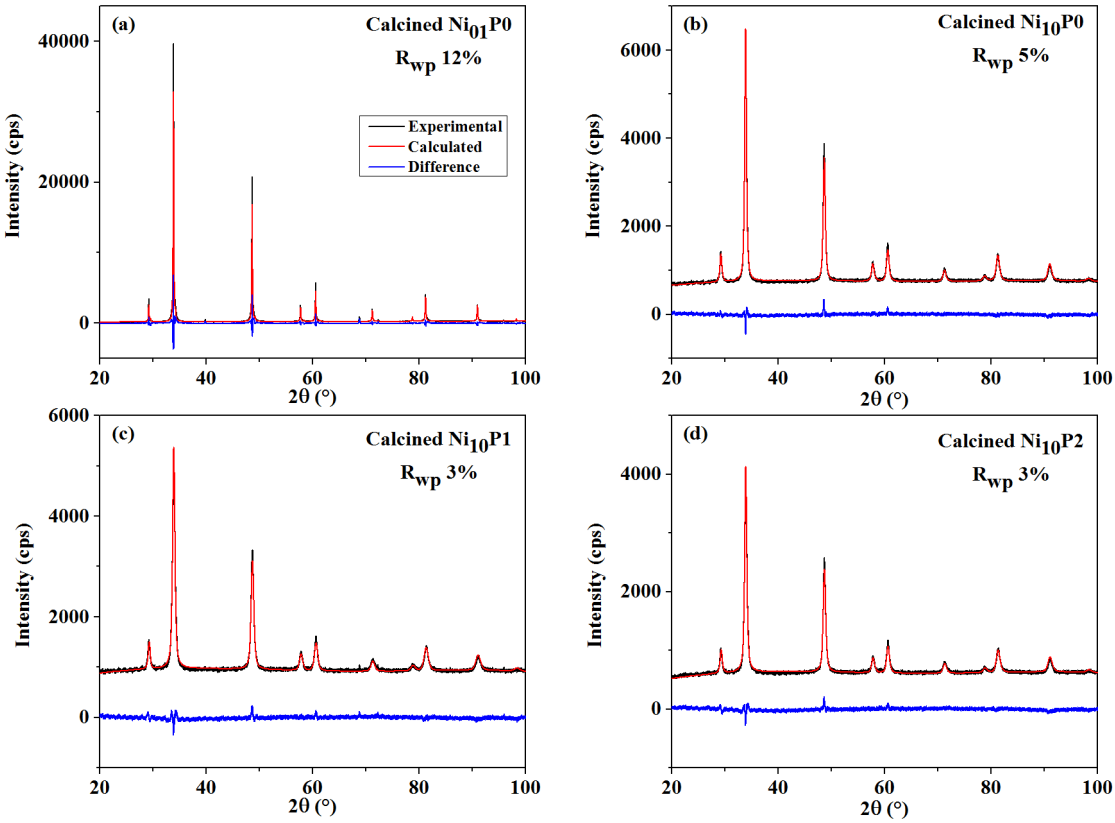

FIGURE S1. XRD patterns of the calcined catalysts performed with synchrotron radiation (10 keV).

(a)

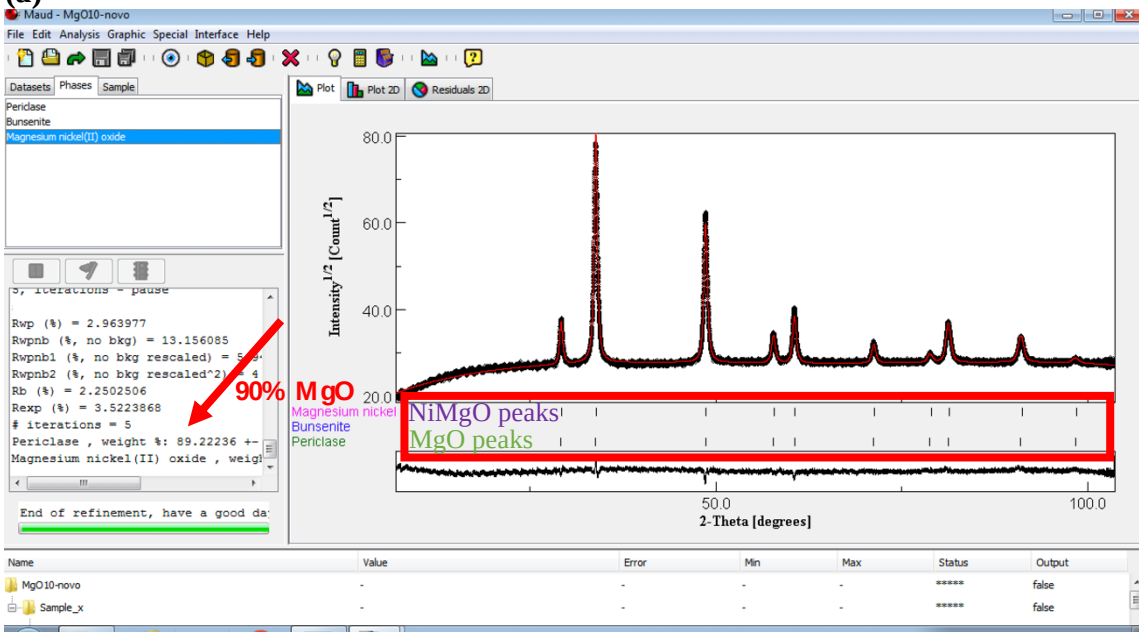

(b)

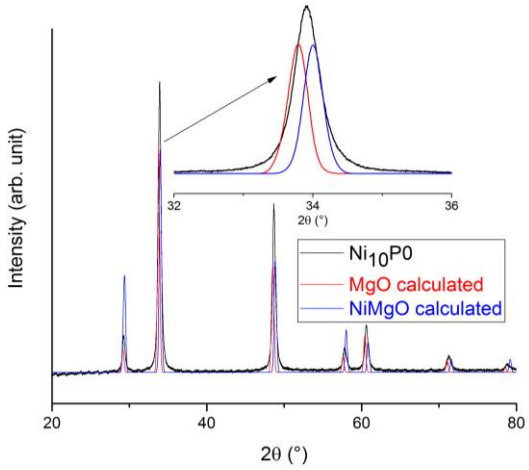

FIGURE S2. (a) Profile of refinement for the $Ni_{10}P0$ sample. (b) Calculated diffractograms for MgO and NiMgO, together with the real diffractogram for $Ni_{10}P0$ performed with synchrotron radiation (10 keV).

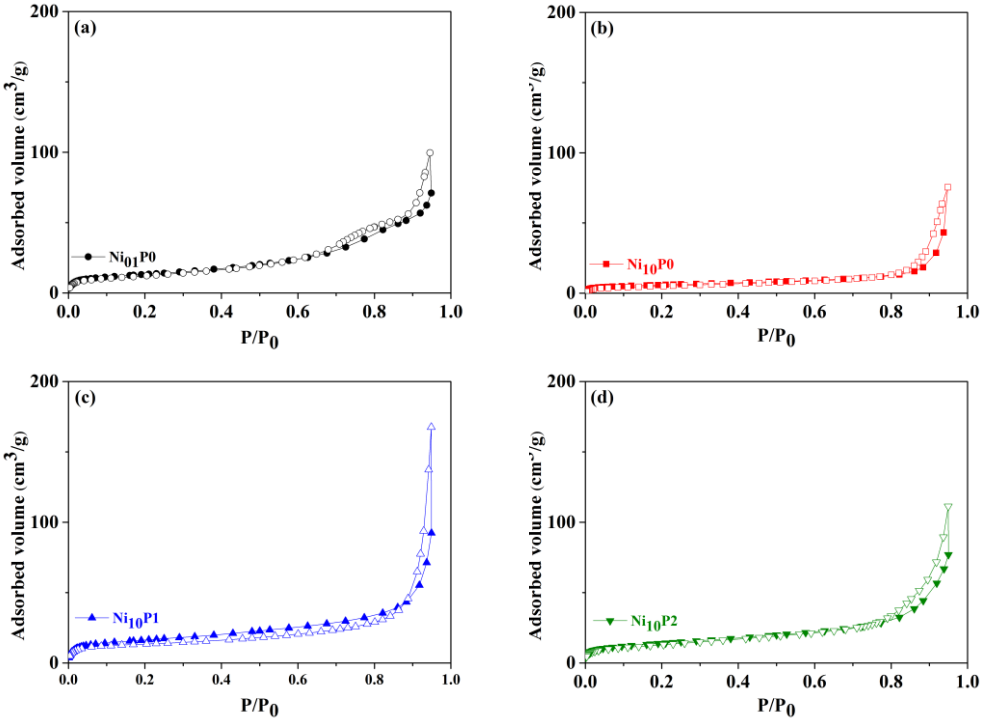

FIGURE S3. Nitrogen adsorption-desorption isotherms for the calcined catalysts.

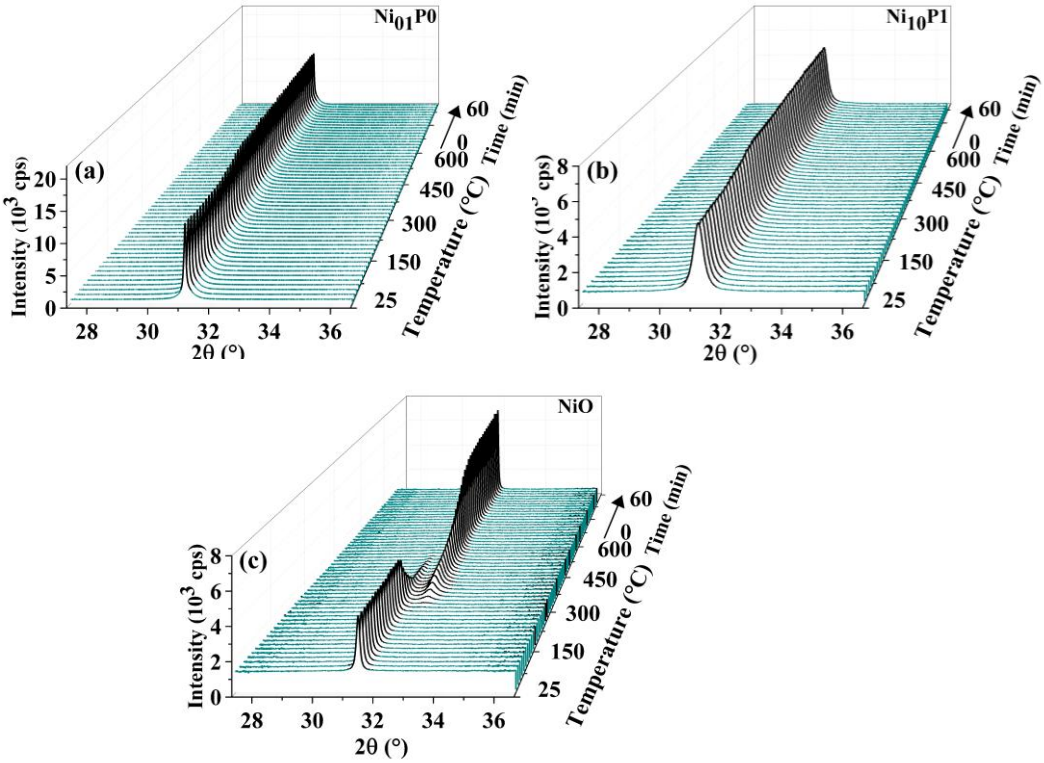

FIGURE S4. *In situ* XRD measurements during thermal activation of (a) $Ni_{01}P0$ and (b) $Ni_{10}P1$, and (c) NiO reference.

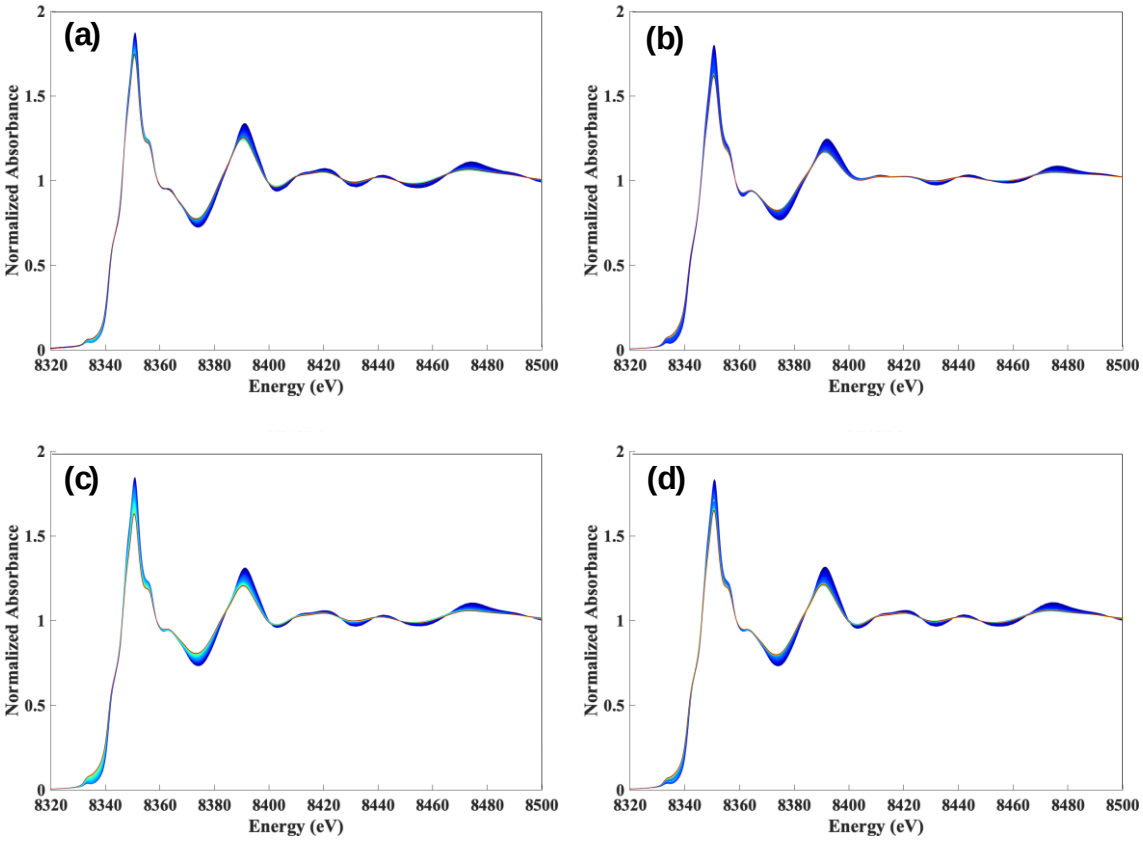

FIGURE S5. X-ray absorption spectra in the XANES region during the thermal activation and 1 h of reaction at 500 °C for (a) $Ni_{01}P0$, (b) $Ni_{10}P0$, (c) $Ni_{10}P1$, and (d) $Ni_{10}P2$.

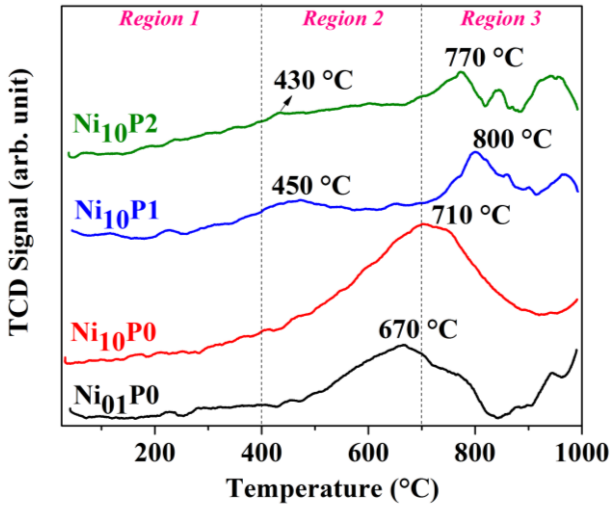

FIGURE S6. TPR profiles of the samples.

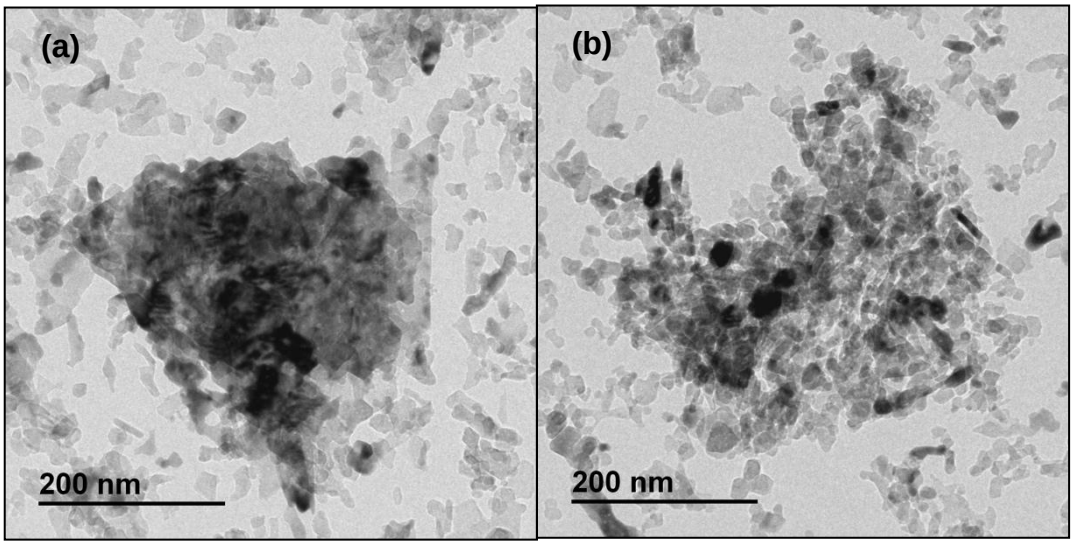

FIGURE S7. Transmission electron micrographs of the reduced catalysts (a) $Ni_{10}P0$ and (b) $Ni_{10}P2$, before the reaction.

Table S1. Structural parameters obtained from fitting of the EXAFS spectra obtained during the steam reforming of ethanol at 500 °C. E_0 = 8347 ± 1.6 eV.

	Atom	**N**	**R (Å)**	**σ^2 (Å^2) (10^{-3})**	**R_F (10^{-3})**
$Ni_{01}P0$	Ni	5.5 ± 1.2	2.49 ± 0.02	6.3 ± 1.9	7.8
	O	5.4 ± 0.1	2.08 ± 0.01	12.8 ± 2.3	
	Ni	0.2 ± 0.2	2.96 ± 0.01	11.8 ± 2.3	
	Mg	11.8 ± 0.2	2.96 ± 0.01	11.8 ± 2.3	
$Ni_{10}P0$	Ni	9.4 ± 1.8	2.45 ± 0.06	13.1 ± 2.2	19.6
	O	5.4 ± 0.1	2.07 ± 0.01	12.9 ± 0.9	
	Ni	4.7 ± 0.3	2.98 ± 0.01	13.6 ± 3.2	
	Mg	7.3 ± 0.3	2.98 ± 0.01	13.6 ± 3.2	
$Ni_{10}P1$	Ni	6.2 ± 0.9	2.51 ± 0.02	13.8 ± 1.2	6.0
	O	4.8 ± 0.1	2.09 ± 0.01	12.4 ± 0.1	
	Ni	0.7 ± 0.3	2.98 ± 0.02	13.2 ± 0.6	
	Mg	11.3 ± 0.3	2.98 ± 0.02	13.2 ± 0.6	
$Ni_{10}P2$	Ni	6.5 ± 0.9	2.50 ± 0.01	14.0 ± 1.5	5.2
	O	4.8 ± 0.1	2.08 ± 0.01	12.3 ± 0.1	
	Ni	0.6 ± 0.3	2.97 ± 0.02	13.3 ± 0.5	
	Mg	11.4 ± 0.3	2.97 ± 0.02	13.3 ± 0.5	

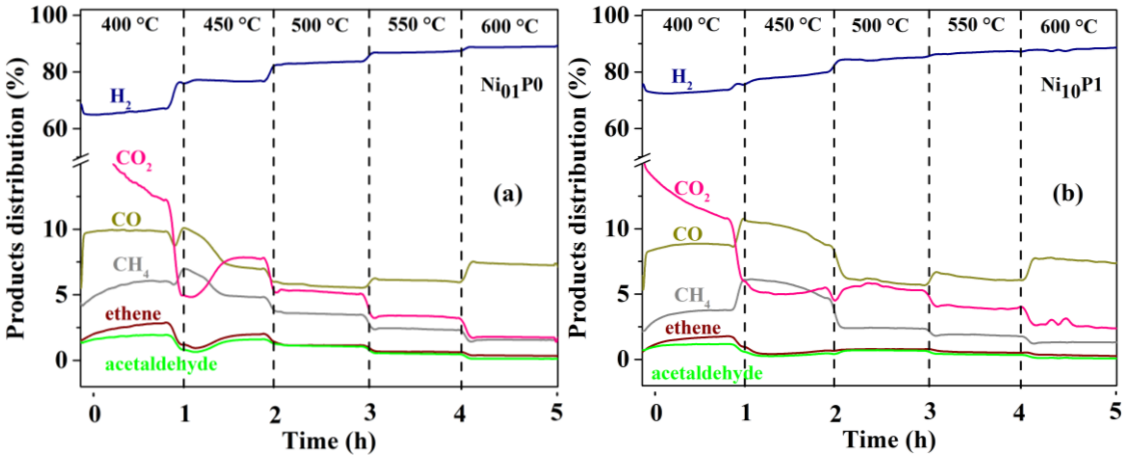

FIGURE S8. Distribution of products during catalytic reaction for (a) $Ni_{01}P0$ and (b) $Ni_{10}P1$.

Table S2. Ethanol steam reforming reaction steps [8].

Reaction	Equation	Feature
Stoichiometric reaction	$C_2H_5OH + 3H_2O \rightleftharpoons 2CO_2 + 6H_2$	Ideal condition
Non-stoichiometric reaction	$C_2H_5OH + H_2O \rightleftharpoons 2CO + 4H_2$ $C_2H_5OH + 2H_2 \rightleftharpoons 2CH_4 + H_2O$	Low H_2 formation
Dehydrogenation	$C_2H_5OH \rightleftharpoons C_2H_4O + H_2$	Steps for H_2 formation
Acetaldehyde decomposition	$C_2H_4O \rightleftharpoons CH_4 + CO$	
Acetaldehyde steam reforming	$C_2H_4O + H_2O \rightleftharpoons 3H_2 + 2CO$	
Dehydration	$C_2H_5OH \rightleftharpoons C_2H_4 + H_2O$	Undesired route, main coke formation
Coke formation	$C_2H_4 \rightleftharpoons$ Coke	
Decomposition	$C_2H_5OH \rightleftharpoons CO + CH_4 + H_2$ $2C_2H_5OH \rightleftharpoons C_3H_6O + CO + 3H_2$ $C_2H_5OH \rightleftharpoons 0.5CO_2 + 1.5CH_4$	
Reactions between products		Coke favoring and low H_2 formation
Methanation	$CO + 3H_2 \rightleftharpoons CH_4 + H_2O$ $CO_2 + 4H_2 \rightleftharpoons CH_4 + 2H_2O$	
Methane decomposition	$CH_4 \rightleftharpoons 2H_2 + C$	
Boudouard Reaction	$2CO \rightleftharpoons CO_2 + C$	
Water-gas shift reaction (WGSR)	$CO + H_2O \rightleftharpoons CO_2 + H_2$	Low coke formation and H_2 selectivity improvement

Table S3. Parameters obtained by the coordination number from fitting of the EXAFS data: cluster order (L), quantity of atoms in the cluster (N_{at}), dispersion (Disp), particle diameter ($D_{Ni\ EXAFS}$), and metallic surface area (S_{met}). The turnover frequency (TOF) was calculated at 500 °C.

Sample	L	N_{at}	Disp. (%)	$D_{Ni\ EXAFS}$ (nm)	S_{met} (m^2/g)	TOF x 10^{-3} (s^{-1})
$Ni_{01}P0$	1	13	92	1.1	0.5	3.0
$Ni_{10}P0$	3.7	252	55	1.6	3.6	1.0
$Ni_{10}P1$	1.2	19	89	1.1	12.1	5.2
$Ni_{10}P2$	1.3	22	87	1.1	10.2	4.9

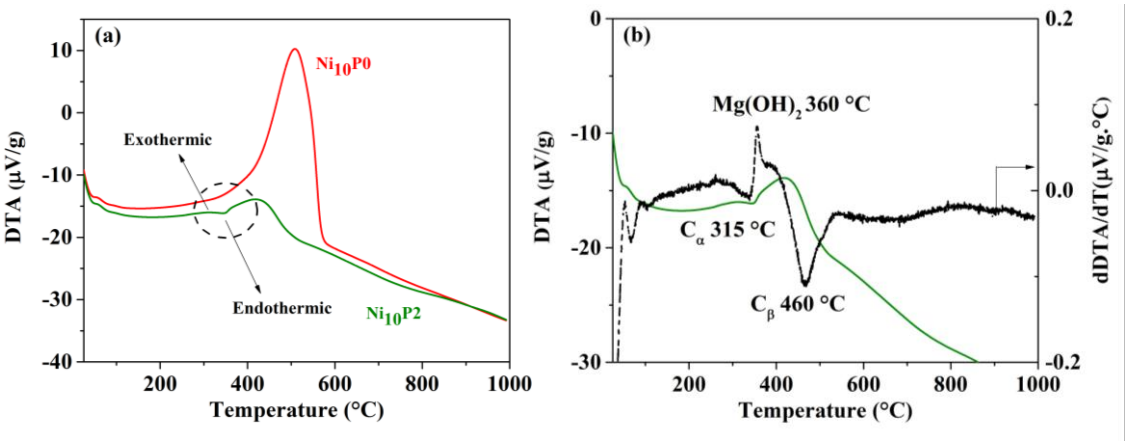

FIGURE S9. (a) DTA analysis of the spent catalysts and (b) derivative of DTA for sample $Ni_{10}P2$.

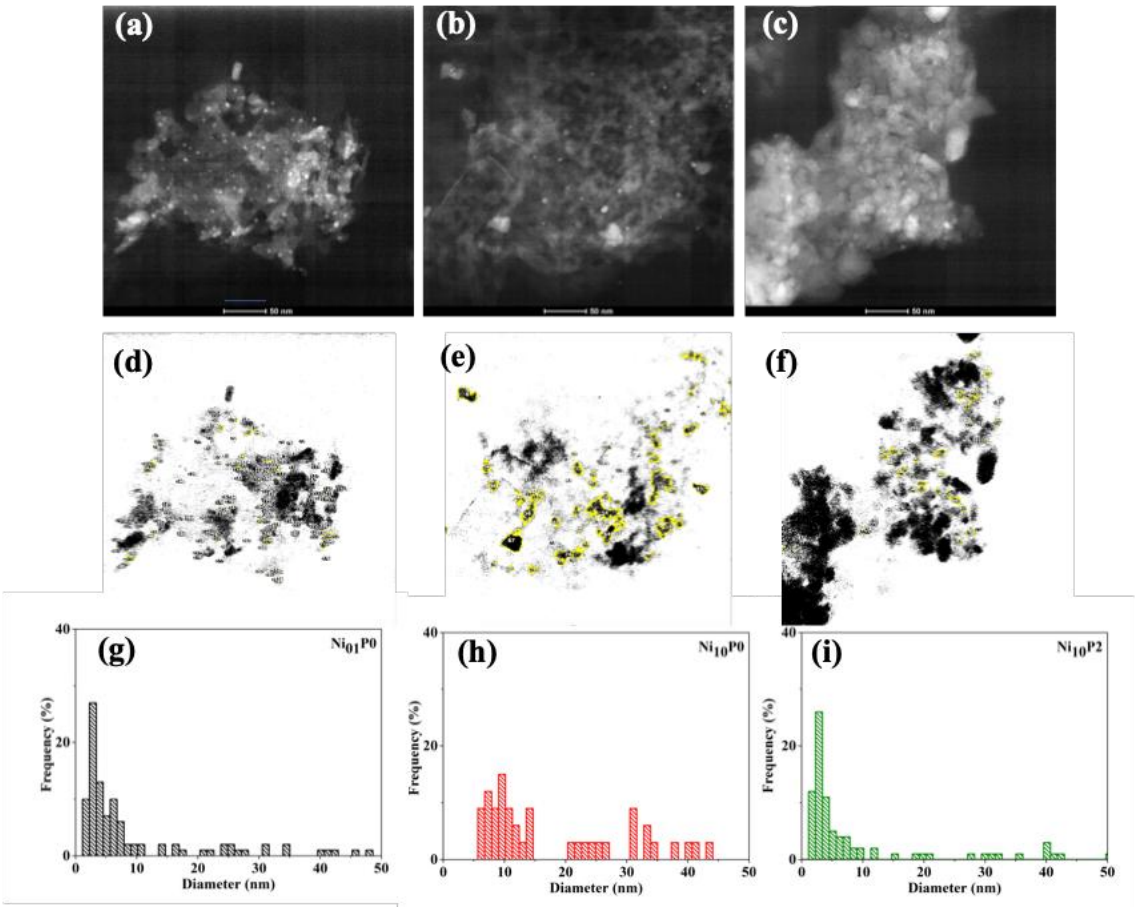

FIGURE S10. Transmission electron micrographs of the spent catalysts (a) $Ni_{01}P0$, (b) $Ni_{10}P0$, and (c) $Ni_{10}P2$; particle mapping for the catalysts (d) $Ni_{01}P0$, (e) $Ni_{10}P0$, and (f) $Ni_{10}P2$; and particle size distributions for (g) $Ni_{01}P0$, (h) $Ni_{10}P0$, and (i) $Ni_{10}P2$.

Table S4. Catalytic activities reported for catalysts similar to those studied in this work, as well as some catalysts with noble metals as the active phase, applied for ethanol steam reforming.

Active phase	Support	Conversion (%)	Selec. H_2 (%)	Temp. (°C)	Reference
Ni	MgOpa	100	68	500	[43]
Ni	CeO_2-MgO	100	70	600	[69]
Ni	MgO-Al_2O_3	100	94	600	[70]
Ni	MgO	100	75	600	[54]
Ni	Li-MgO	90	91	650	[73]
Ni	MgO	70	95	650	[71]
Ni	MgO-CaO	100	97	600	[74]
Ni	MgO-SBA	55	85	600	[75]
Ni	MgO-SBA	95	90	700	[75]
Rh	MgO	100	90	650	[71]
Pd	MgO	60	60	650	[71]
Ru	CeO_2	90	70	450	[72]
Ni	MgO	100	80	600	This study